1

Three-dimensional interaction between uniform current and a submerged horizontal cylinder in an ice-covered channel

Y. F. Yang[1], G. X. Wu[1]† and K. Ren[1]

[1]Department of Mechanical Engineering, University College London, Torrington Place, London WC1E 7JE, UK

The problem of interaction of a uniform current with a submerged horizontal circular cylinder in an ice-covered channel is considered. The fluid flow is described by linearized velocity potential theory and the ice sheet is treated as a thin elastic plate. The potential due to a source or the Green function satisfying all boundary conditions apart from that on the body surface is first derived. This can be used to derive the boundary integral equation for a body of an arbitrary shape. It can also be used to obtain the solution due to multipoles by differentiating the Green function with its position directly. For a transverse circular cylinder, through distributing multipoles along its centre line, the velocity potential can be written in an infinite series with unknown coefficients, which can be determined from the impermeable condition on body surface. A major feature here is that different from the free surface problem, or a channel without the ice sheet cover, this problem is fully three dimensional because of the constraints along the intersection of the ice sheet with the channel wall. It has been also confirmed that there is an infinite number of critical speeds. Whenever the current speed passes a critical value, the force on the body and wave pattern change rapidly, and two more wave components are generated at the far-field. Extensive results are provided for hydroelastic waves and hydrodynamic forces when the ice sheet is under different edge conditions, and the insight of their physical features is discussed.

---

1. Introduction

In ocean engineering and naval architecture, it is common to undertake model tests in a wave/towing tank. It can be expected that if the width of the tank is not sufficiently larger than the structure dimension of the model or the wavelength, it can greatly affect the interactions between the fluid flow and the structure. The measured result may not truly reflect that of the prototype in the real ocean. Furthermore, the tank has its natural frequencies, at which resonance of the fluid motion can occur. Such a resonance due to the side wall effect on the other hand does not occur in the ocean. It is then important to understand how the tank wall affects the desired results. Therefore, there has been an extensive amount of work

† Email address for correspondence: g.wu@ucl.ac.uk

on body / flow / tank or channel interactions. By employing linearized velocity potential theory, Linton (1993) derived the Green function for free surface wave in a channel. The diffraction/radiation and the forward speed problem of a submerged sphere in a channel were studied by Wu (1998a,b) where multipole expansion was applied. In addition to submerged bodies, wave interaction with surface piercing structures in a channel was also well studied. Linton et al. (1992) provided an analytical solution for wave diffraction and radiation by a vertical circular cylinder using cylindrical system. Later, Evans & Porter (1997) and Utsunomiya & Eatock Taylor (1999) solved wave diffraction by multiple cylinders and discussed the effect of trapped mode (Ursell 1951). A more recent work by Newman (2017) provided some detailed description of the trapped mode phenomenon in a channel for various structures, including submerged bodies and bottom-mounted cylinders with different cross sections.

In recent years, there has been an increasing interest in the hydrodynamic problems in polar and other icy water regions. One of the typical features in these regions is the ice in many different forms, one of which is ice sheet covering water surface over very large extent. In the experiment, the ice sheet will meet the tank wall. At their intersection, the physical constrain of the ice sheet edge, including whether the edge is clamped, simply supported or free, can significantly affect the result. In fact, it has been shown in Korobkin et al. (2014) and Ren et al. (2020) that while the transverse modes of the fluid flow are mathematically orthogonal, they are still completely coupled. One consequence of this coupling is that unlike the free surface problem, the purely two-dimensional wave propagating along the channel is impossible when there is an ice sheet cover. The work by Ren et al. (2020) is mainly for wave propagation without any structures in its path, although the case of an ice sheet with a crack is considered. Here we shall consider a problem of a body submerged in a channel below an ice sheet in a uniform current. This is similar to a submerged body moving forward with constant speed. Although the problem may seem to be conventional for the free surface flow, when there is an ice sheet the physics of the fluid flow and the resistance and lift on the body is very different. The present work aims to shed some light into this.

When there is no channel wall, or for the open ice sheet problem, there has been a large volume of work on interactions of fluid flow and ice sheet. In mathematical modelling, the ice sheet is treated as a thin elastic plate and the fluid flow is described by the linearized velocity potential theory. A review of some early works based on this method can be found in Squire (2007). Typical three-dimensional works on wave interaction with ice sheets/floes include those by Fox & Squire (1994) and Balmforth & Craster (1999) for oblique wave diffraction by a semi-infinite ice sheet, Meylan & Squire (1996) for wave interaction with a circular ice floe, Bennetts & Williams (2010) for wave diffraction by an ice floe of arbitrary shapes, and by Porter (2019) for wave interaction with a rectangular ice floe floating on ocean. There are also works on imperfect ice sheets including cracks, such as Evans & Porter (2003) for hydroelastic waves propagating by a single straight-line crack, and Porter & Evans (2007) for multiple straight-line cracks parallel to each other, and a recent work by Li et al. (2020c) for multiple cracks with arbitrary shapes on ice sheet.

The work mentioned above is mainly about interaction between wave and ice sheet. In polar engineering, it is also important to consider their interaction with structures. For three-dimensional submerged bodies, Das & Mandal (2008) studied wave radiation by a submerged sphere in a fluid with an ice-cover by multipole expansion method. Sturova (2013) derived the time domain Green function due to a source undergoing arbitrary three-dimensional motion in water below an ice sheet with infinite extent, and further considered the wave radiation by a submerged sphere with a forward speed. For wave interaction with structures piercing ice plate or water surface, Brocklehurst et al. (2011) investigated the diffraction problem of hydroelastic wave beneath ice sheet by a single bottom-mounted circular cylinder based on

the Weber transform. Later, Dişibüyük *et al.* (2020) further extended it to vertical cylinder of non-circular cross section by applying the perturbation method at the mean position of the section. Hydroelastic wave diffraction problems by multiple vertical cylinders are solved by Ren *et al.* (2018*a*). When the ice sheet is not directly contacted with the surface of the structures, such as structures are located in a polynya or open water confined by ice sheets, mixed upper surface boundary conditions need to be considered. Ren *et al.* (2018*b*) investigated wave diffraction and radiation by a vertical circular cylinder standing arbitrarily in a circular polynya, while Li *et al.* (2020*a*) employed a hybrid numerical method and considered floating structure of arbitrary shapes in a polynya with various shapes.

Compared with unbounded sea covered by an ice sheet, the hydrodynamic features in an ice-covered channels are quite different. Korobkin *et al.* (2014) studied hydroelastic wave propagating along a rectangular channel with homogeneous ice cover clamped to the side walls. The velocity potential and ice sheet deflection are first expanded into different eigenfunctions. Each term in the expression of the ice sheet deflection satisfies the edge condition and is further expanded into Fourier series used for the velocity potential. The dispersion relations of the channel can be obtained through finding non-trivial solutions of the homogeneous linear equations. Based on the procedure of Korobkin *et al.* (2014), Shishmarev *et al.* (2016) and Khabakhpasheva *et al.* (2019) investigated the hydroelastic waves due to a load moving with a constant speed along a frozen channel through frequency domain and time domain methods, respectively. However, their results and conclusion are only for the clamped edges. Ren *et al.* (2020) explicitly discussed the merit and weakness of the method in Korobkin *et al.* (2014), and then they proposed a more efficient and flexible approach to investigate the propagation of hydroelastic waves in a channel with an ice cover subject to various edge constrains at the side walls, and also the effect of a longitudinal line crack on the ice. In their work, both the velocity potential and the fourth transverse-derivative of the ice deflection are expanded into a series of cosine functions in the transverse direction. The expression of deflection itself is obtained through integration, which contains a series of cosine functions and a quartic polynomial with four additional unknown constants. Using the kinematic and dynamic conditions on the ice sheet, the system of linear equations in terms of these four constants can be obtained by imposing edge conditions at the channel wall. Based on this method, the solution procedure is very much simplified, and it is very convenient to consider different combinations of edge conditions and the effect of the crack.

In the present work, the interaction of a uniform current with a submerged body in an ice-covered rectangular channel is considered. The three-dimensional Green function, or the velocity potential due to a source is first derived. This can then be used to derive the integral equation over the body surface of arbitrary shapes. In particular, we shall consider a submerged horizontal circular cylinder with its axis in the transverse direction. Multipole (Ursell 1949, 1950) is distributed along the centre line. As a result, the velocity potential can be written explicitly in terms of basic and special functions, involving integrals and unknown coefficients which can be obtained from the impermeable condition on the body surface. For the two-dimensional free surface case, the problem of current passing a submerged cylinder has been considered extensively. Lamb (1932) used an approximation where the linearized free surface boundary condition is satisfied exactly but the body surface boundary conditions approximately. Havelock (1936) solved the linear problem exactly in the sense the infinite series can be truncated at a sufficiently large number to achieve the desired accuracy. Tuck (1965) considered the second-order effects, while Haussling & Coleman (1979), Scullen & Tuck (1995) and Semenov & Wu (2020) further solved the fully nonlinear problem. However, with the ice sheet, this will be a fully three-dimensional problem and the flow is much more complex. In particular, there will be an infinite number of critical speeds, and multi-wave components at both sides of the channel. Based on the dispersion relationship, extensive
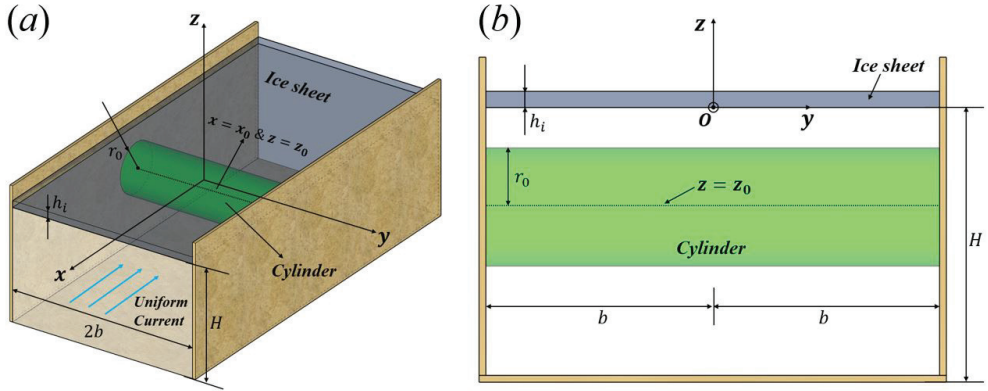
Figure 1: Sketch of the problem. (*a*) Three-dimensional view; (*b*) A cross section view of the channel in the negative $x-$direction.

analyses are made for the physical behaviours of the deflection of the ice cover and the hydrodynamic forces on the cylinder. Compared with the two-dimensional case, it is found that the confined channel walls and the constraints at the ice edge have a significant influence on the hydrodynamic features.

The paper is arranged as follows. The governing equation and boundary conditions for a submerged horizontal circular cylinder in an ice-covered channel in current is presented in Section 2. The Green function or potential due to a single source is derived in Section 3.1. The multipole expansion is constructed in Section 3.2. The formulas of hydrodynamic forces on the cylinder and ice deflection are obtained in sections Section 3.3 and Section 3.4 respectively. The numerical procedure is briefly introduced in Section 3.5. The numerical results are shown in Section 4, followed by the conclusions in Section 5. The expression of some essential coefficients is given in Appendix A. The symmetry property of the Green function is proved in Appendix B, while the far-field formula of the resistance is derived in Appendix C.

2. Governing Equation and boundary conditions

We consider the problem of a horizontal circular cylinder submerged in an infinitely long rectangular channel covered by an ice sheet. A sketch of the problem is shown in figure 1. The channel has half-width b and calm water depth H. The density and thickness of the homogeneous ice sheet are assumed to be constant and represented by ρ_i and h_i respectively, and the density of the water is ρ. A Cartesian coordinate system $O - xyz$ is defined with the origin located on the central line of the water surface, the $x-$axis along the longitudinal direction of the channel, and $z-$axis pointing upwards. The centre line of the cylinder is located at $x = x_0$ & $z = z_0$ and its radius is equal to r_0.

It is assumed that the fluid is ideal, incompressible, its motion is irrotational, and the linearized velocity potential theory is employed. As discussed in the introduction, due to the ice sheet and its edge conditions, the problem will be three dimensional. The total velocity potential is written as

$$\Phi = -Ux + \phi, \tag{2.1}$$

where U denotes the velocity of the uniform current from $x = +\infty$, $\phi(x, y, z, t)$ is the disturbed velocity potential by the cylinder, which satisfies the Laplace equation in the entire

168   fluid domain,

$$\nabla^2\phi = \frac{\partial^2\phi}{\partial x^2} + \frac{\partial^2\phi}{\partial y^2} + \frac{\partial^2\phi}{\partial z^2}, \quad -\infty < x < +\infty, \ -b \leqslant y \leqslant b, \ -H \leqslant z \leqslant 0. \tag{2.2}$$

170   The deflection of the ice plate $\eta(x, y, t)$ should satisfy the Euler-Bernoulli equation on $z = 0$,

$$\rho_i h_i \eta_{tt} + L\nabla^4\eta = p, \quad z = 0, \tag{2.3}$$

172   where $L = Eh_i^3/\left[12\left(1 - \nu^2\right)\right]$ denotes the flexural rigidity of the ice sheet, E and ν represent
173   its Young's modulus and Poisson's ratio respectively. The fluid pressure p on the right-hand
174   side of (2.3) is the excessive fluid pressure and does not include the weight of ice. It can be
175   calculated through the linearized Bernoulli equation

$$p = -\rho\left(\frac{\partial\phi}{\partial t} - U\frac{\partial\phi}{\partial x} + g\eta\right), \quad z = 0, \tag{2.4}$$

177   where g is the acceleration due to gravity. The kinematic boundary condition can be written
178   as

$$\left(\frac{\partial}{\partial t} - U\frac{\partial}{\partial x}\right)\eta = \frac{\partial\phi}{\partial z}, \quad z = 0. \tag{2.5}$$

180   For steady flow, $\partial/\partial t = 0$. We have

$$\left(L\nabla^4 + \rho g\right)\eta = \rho U\frac{\partial\phi}{\partial x}, \quad z = 0, \tag{2.6}$$

182

$$-U\frac{\partial\eta}{\partial x} = \frac{\partial\phi}{\partial z}, \quad z = 0, \tag{2.7}$$

184   in which (2.6) is obtained by substituting (2.4) into (2.3). The impermeable condition on the
185   cylinder surface S_B can be written as

$$\frac{\partial\phi}{\partial n} = Un_x, \quad \text{on } S_B, \tag{2.8}$$

187   where $\boldsymbol{n} = (n_x, 0, n_z)$ is the unit normal vector of S_B, which is pointing out of the fluid
188   domain. Similarly, the impermeable boundary conditions on the rigid side walls and bottom
189   of the channel can be expressed as

$$\frac{\partial\phi}{\partial y} = 0, \quad y = \pm b, \tag{2.9}$$

191

$$\frac{\partial\phi}{\partial z} = 0, \quad z = -H. \tag{2.10}$$

193   Different from free surface problems, there are also edge conditions at intersection lines of
194   the ice sheet with the two side walls, or $y = \pm b, z = 0$, which can be written as (Timoshenko
195   & Woinowsky-Krieger 1959)

$$\left.\begin{array}{ll} \eta = 0, \quad \dfrac{\partial\eta}{\partial y} = 0, & \text{Clamped edge} \\[2mm] \eta = 0, \quad \dfrac{\partial^2\eta}{\partial y^2} + \nu\dfrac{\partial^2\eta}{\partial x^2} = 0, & \text{Simply supported edge} \\[2mm] \dfrac{\partial^2\eta}{\partial y^2} + \nu\dfrac{\partial^2\eta}{\partial x^2} = 0, \quad \dfrac{\partial^3\eta}{\partial y^3} + (2-\nu)\dfrac{\partial^3\eta}{\partial x^2\partial y} = 0, & \text{Free edge} \end{array}\right\}. \tag{2.11}$$

6

197   The radiation condition at far-field $x \to \pm\infty$ can be written as

198
$$\frac{\partial \phi}{\partial x} = \mathcal{U}_{\pm}(x, y, z), \quad x \to \pm\infty, \tag{2.12}$$

199   where $\mathcal{U}_{\pm}(x, y, z)$ represents waves generated by the cylinder. The waves can have multi
200   components and group velocities of the waves at $x \to +\infty$ and $x \to -\infty$ are larger and
201   smaller than U respectively. This will be discussed in detail later.

3. Solution procedures

3.1. *The Green function: velocity potential due to a single source*

204   The Green function $G(x, y, z, x_0, y_0, z_0)$ is the velocity potential at point $P(x, y, z)$ due to
205   a source at $P_0(x_0, y_0, z_0)$, which satisfies the following equation,

206
$$\nabla^2 G = \delta(x - x_0)\delta(y - y_0)\delta(z - z_0), \tag{3.1}$$

207   where $\delta(x)$ is the Dirac delta-function. $\xi(x, y, x_0, y_0, z_0)$ is defined as the wave elevation at
208   point (x, y) induced by the source at $P_0(x_0, y_0, z_0)$. $G(x, y, z, x_0, y_0, z_0)$ and $\xi(x, y, x_0, y_0, z_0)$
209   also need to satisfy the boundary conditions (2.6), (2.7) and (2.9)~(2.12).

210   Performing the Fourier transform for G and ξ in the x−direction

211
$$\left. \begin{aligned} \hat{G} &= \int_{-\infty}^{+\infty} G e^{-ikx} dx \\ \hat{\xi} &= \int_{-\infty}^{+\infty} \xi e^{-ikx} dx \end{aligned} \right\}. \tag{3.2}$$

212   and applying (3.2) to (3.1), we have

213
$$-k^2 \hat{G} + \frac{\partial^2 \hat{G}}{\partial y^2} + \frac{\partial^2 \hat{G}}{\partial z^2} = \delta(y - y_0)\delta(z - z_0)e^{-ikx_0}. \tag{3.3}$$

214   Based on the impermeable condition in (2.9), $\hat{G}$ can be further expanded into an orthogonal
215   series of cosine functions in the y−direction. Using the condition in (2.10), the solution of
216   (3.3) can be written in the following form

217
$$\hat{G} = \sum_{n=0}^{+\infty} Z_n(k, z, x_0, y_0, z_0) \cos \sigma_n(y + b), \tag{3.4}$$

218   where

219
$$\begin{aligned} Z_n(k, z, x_0, y_0, z_0) = &-\frac{\left[e^{-K_n |z - z_0|} + e^{-K_n(z + z_0 + 2H)} \right] e^{-ikx_0} \cos \sigma_n(y_0 + b)}{2(1 + \delta_{n0})bK_n} \\ &+ b_n \frac{e^{-ikx_0} \cosh K_n(z + H)}{\cosh K_n H} \end{aligned} \tag{3.5}$$

220   $\sigma_n = n\pi/2b$, $K_n = \sqrt{k^2 + \sigma_n^2}$, and δ_{ij} denotes the Kronecker delta function. The terms of b_n
221   in (3.5) correspond to the general solution of (3.3) when the right-hand side is zero. b_n are
222   to be determined by the conditions on the ice sheet. Applying Fourier transform to (2.6) and
223   (2.7), we have

224
$$(\rho g + Lk^4)\hat{\xi} - 2Lk^2 \frac{\partial^2 \hat{\xi}}{\partial y^2} + L \frac{\partial^4 \hat{\xi}}{\partial y^4} = ik\rho U \hat{G}, \tag{3.6}$$

225

$$-\mathrm{i}kU\hat{\xi} = \frac{\partial \hat{G}}{\partial z}. \tag{3.7}$$

We choose to follow the approach taken by Ren *et al.* (2020), which involves expanding $\partial^4 \hat{\xi}/\partial y^4$ rather than $\hat{\xi}$ into a cosine series, thus

$$\frac{\partial^4 \hat{\xi}}{\partial y^4} = e^{-\mathrm{i}kx_0} \sum_{n=0}^{+\infty} a_n \cos \sigma_n(y + b). \tag{3.8}$$

Then through integration four times, $\hat{\xi}$ can be obtained as

$$\hat{\xi} = e^{-\mathrm{i}kx_0} \left[c_0 + c_1 y + c_2 y^2 + c_3 y^3 + \frac{a_0}{24} y^4 + \sum_{n=1}^{+\infty} \frac{a_n}{\sigma_n^4} \cos \sigma_n(y + b) \right], \tag{3.9}$$

where a_n ($n = 0, 1, 2...$) are unknown coefficients and are functions of k, c_i ($i = 0 \sim 3$) are four constants which can be linked to a_n through edge conditions. It should be mentioned here that c_0, c_2 and a_{2n} correspond to symmetric component, while c_1, c_3 and a_{2n+1} correspond to anti-symmetric component. Substituting (3.4), (3.5) and (3.9) into (3.6) and (3.7), we have

$$(\rho g + Lk^4) \left[c_0 + c_1 y + c_2 y^2 + c_3 y^3 + \frac{a_0}{24} y^4 + \sum_{n=1}^{+\infty} \frac{a_n}{\sigma_n^4} \cos \sigma_n(y + b) \right]$$

$$- 2k^2 L \left[2c_2 + 6c_3 y + \frac{a_0}{2} y^2 - \sum_{n=1}^{+\infty} \frac{a_n}{\sigma_n^2} \cos \sigma_n(y + b) \right] + L \sum_{n=0}^{+\infty} a_n \cos \sigma_n(y + b) \tag{3.10}$$

$$= \mathrm{i}k\rho U \sum_{n=0}^{+\infty} \left[-\frac{e^{-K_n H} \cosh K_n(z_0 + H)}{(1 + \delta_{n0}) b K_n} \cos \sigma_n(y_0 + b) + b_n \right] \cos \sigma_n(y + b),$$

237

$$-\mathrm{i}kU \left[c_0 + c_1 y + c_2 y^2 + c_3 y^3 + \frac{a_0}{24} y^4 + \sum_{n=1}^{+\infty} \frac{a_n}{\sigma_n^4} \cos \sigma_n(y + b) \right]$$

$$= \sum_{n=0}^{+\infty} \left[\frac{e^{-K_n H} \cosh K_n(z_0 + H)}{(1 + \delta_{n0}) b} \cos \sigma_n(y_0 + b) + b_n K_n \tanh K_n H \right] \cos \sigma_n(y + b). \tag{3.11}$$

The term y^j ($j = 0 \sim 4$) can be further expanded into the orthogonal series of cosine functions as

$$y^j = \sum_{n=0}^{+\infty} d_n^{(j)} \cos \sigma_n(y + b). \tag{3.12}$$

Then, (3.10) and (3.11) can be written as

$$(\rho g + Lk^4) \left[c_0 d_n^{(0)} + c_1 d_n^{(1)} + c_2 d_n^{(2)} + c_3 d_n^{(3)} + \frac{a_0}{24} d_n^{(4)} + \frac{(1 - \delta_{n0}) a_n}{\sigma_n^4} \right]$$

$$- 2k^2 L \left[2c_2 d_n^{(0)} + 6c_3 d_n^{(1)} + \frac{a_0}{2} d_n^{(2)} - \frac{(1 - \delta_{n0}) a_n}{\sigma_n^2} \right] + La_n \tag{3.13}$$

$$= \mathrm{i}k\rho U \left[-\frac{e^{-K_n H} \cosh K_n(z_0 + H)}{(1 + \delta_{n0}) b K_n} \cos \sigma_n(y_0 + b) + b_n \right], \quad n = 0, 1, 2...$$

$$-\mathrm{i}kU\left[c_0d_n^{(0)} + c_1d_n^{(1)} + c_2d_n^{(2)} + c_3d_n^{(3)} + \frac{a_0}{24}d_n^{(4)} + \frac{(1-\delta_{n0})a_n}{\sigma_n^4}\right]$$

$$= \left[\frac{e^{-K_nH}\cosh K_n(z_0+H)}{(1+\delta_{n0})b}\cos\sigma_n(y_0+b) + b_nK_n\tanh K_nH\right], \quad n = 0, 1, 2... \tag{3.14}$$

From (3.13) and (3.14), a_n and b_n can be expressed as

$$a_n = \alpha_{n,0}c_0 + \alpha_{n,1}c_1 + \alpha_{n,2}c_2 + \alpha_{n,3}c_3 + \mathrm{i}R_n, \quad n = 0, 1, 2... \tag{3.15}$$

$$b_n = \frac{1}{K_n\tanh K_nH}\left(\mathrm{i}\beta_{n,0}c_0 + \mathrm{i}\beta_{n,1}c_1 + \mathrm{i}\beta_{n,2}c_2 + \mathrm{i}\beta_{n,3}c_3 + S_n\right), \quad n = 0, 1, 2... \tag{3.16}$$

where

$$\alpha_{n,j} = \frac{1}{\Delta_n}\left\{\begin{array}{l} d_n^{(j)}\left[(\rho g + Lk^4)K_n\tanh K_nH - \rho k^2U^2\right] \\ -4\delta_{2j}k^2Ld_n^{(0)}K_n\tanh K_nH - 12\delta_{3j}k^2Ld_n^{(1)}K_n\tanh K_nH\end{array}\right\} + (1-\delta_{n0})\gamma_n\alpha_{0,j}, \tag{3.17a}$$

$$\beta_{n,j} = -Uk\left[d_n^{(j)} + \frac{d_n^{(4)}}{24}\alpha_{0,j} + \frac{(1-\delta_{n0})}{\sigma_n^4}\alpha_{n,j}\right], \qquad j = 0 \sim 3 \tag{3.17b}$$

and

$$R_n = \frac{\rho Uk\cosh K_n(z_0+H)\cos\sigma_n(y_0+b)}{(1+\delta_{n0})b\Delta_n\cosh K_nH} + (1-\delta_{n0})\gamma_nR_0, \tag{3.18a}$$

$$S_n = kU\left(\frac{d_n^{(4)}}{24}R_0 + \frac{1-\delta_{n0}}{\sigma_n^4}R_n\right) - \frac{e^{-K_nH}\cosh K_n(z_0+H)\cos\sigma_n(y_0+b)}{(1+\delta_{n0})b}, \tag{3.18b}$$

with

$$\Delta_n = \left\{\begin{array}{l}\delta_{n0}\left[-\left(\dfrac{\rho g + Lk^4}{24}d_n^{(4)} - k^2Ld_n^{(2)} + L\right)K_n\tanh K_nH + \dfrac{\rho k^2U^2d_n^{(4)}}{24}\right] \\ +(1-\delta_{n0})\left[-\left(\dfrac{\rho g + Lk^4}{\sigma_n^4} + \dfrac{2k^2L}{\sigma_n^2} + L\right)K_n\tanh K_nH + \dfrac{\rho k^2U^2}{\sigma_n^4}\right]\end{array}\right\}, \tag{3.19a}$$

$$\gamma_n = \frac{1}{\Delta_n}\left[\left(\frac{\rho g + Lk^4}{24}d_n^{(4)} - k^2Ld_n^{(2)}\right)K_n\tanh K_nH - \frac{\rho k^2U^2d_n^{(4)}}{24}\right]. \tag{3.19b}$$

If we consider the symmetry or anti symmetry nature of y^j ($j = 0 \sim 3$), we will have $d_{2n}^{(2j+1)} = d_{2n+1}^{(2j)} = 0$ ($j = 0, 1$). This leads to $\gamma_{2n+1} = 0$ and $\alpha_{2n+1,2j} = \alpha_{2n,2j+1} = 0$ ($j = 0, 1$, $n \geqslant 0$). As a result, a_n can be further expressed as

$$\left.\begin{array}{l}a_{2n} = \alpha_{2n,0}c_0 + \alpha_{2n,2}c_2 + \mathrm{i}R_{2n} \\ a_{2n+1} = \alpha_{2n+1,1}c_1 + \alpha_{2n+1,3}c_3 + \mathrm{i}R_{2n+1}\end{array}\right\}. \tag{3.20}$$

It can be seen from (3.20) that a_{2n} depend on two unknown coefficients c_0 and c_2, while a_{2n+1} depend on c_1 and c_3. b_n can be also treated in a similar way. The four unknown coefficients c_i ($i = 0 \sim 3$) can be determined from the four edge conditions, including those in (2.11). As a result, a system of linear equations of the following form can be established,

$$[\mathcal{A}][C] = [\mathcal{B}], \tag{3.21}$$

where $[\mathcal{A}]$ is a 4×4 coefficient matrix, $[C]$ is a column containing c_i, and $[\mathcal{B}]$ is a known

272 column. For a specific case, this 4×4 matrix equation may be further simplified. If the edge
273 conditions at $y = \pm b$ are same, (3.21) may be split into two independent 2×2 submatrix
274 equations, one for c_0 and c_2, and the other for c_1 and c_3. As a result, the symmetric and
275 anti-symmetric transverse waves in (3.9) become independent to each other. In general, c_i
276 ($i = 0 \sim 3$) are fully coupled to each other, which leads a_{2n} and a_{2n+1} in (3.20) to become
277 coupled. The solution of c_i can be written as

$$c_i = -\mathrm{i} \sum_{m=0}^{+\infty} \frac{\rho U k \cosh K_m(z_0 + H) \cos \sigma_m(y_0 + b)}{(1 + \delta_{m0})b|\mathcal{A}|\Delta_m \cosh K_m H} c'_{m,i}, \quad i = 0 \sim 3, \qquad (3.22)$$

279 where $|\mathcal{A}|$ is the determinant of $[\mathcal{A}]$. The elements of $[\mathcal{A}]$ and $[\mathcal{B}]$, as well as coefficient
280 $c'_{m,i}$ are related to edge conditions, an example of these under clamped-clamped edges are
281 given in appendix A.
282   Once c_i ($i = 0 \sim 3$), a_n and b_n ($n = 0, 1, 2...$) are obtained, then G and ξ can be obtained
283 through the inverse Fourier transform. Using (Linton & McIver 2001)

$$\int_{-\infty}^{+\infty} \frac{\delta_{n0}e^{-K_n H} - e^{-K_n|z-z_0|+\mathrm{i}k(x-x_0)}}{2K_n} dk = \delta_{n0} \ln\left(\frac{r}{H}\right) - (1 - \delta_{n0})\mathcal{K}_0(\sigma_n r), \qquad (3.23a)$$

$$\int_{-\infty}^{+\infty} \frac{\delta_{n0}e^{-K_n H} - e^{-K_n(z+z_0+2H)+\mathrm{i}k(x-x_0)}}{2K_n} dk = \delta_{n0} \ln\left(\frac{r'}{H}\right) - (1 - \delta_{n0})\mathcal{K}_0(\sigma_n r'), \quad (3.23b)$$

287 where $r = \sqrt{(x - x_0)^2 + (z - z_0)^2}$ and $r' = \sqrt{(x - x_0)^2 + (z + z_0 + 2H)^2}$, $\mathcal{K}_n$ denotes the
288 nth-order modified Bessel function of second kind. We have the Green function

$$G(x, y, z, x_0, y_0, z_0) = \sum_{n=0}^{+\infty} \mathcal{Z}_n(x, z, x_0, y_0, z_0) \cos \sigma_n(y + b), \qquad (3.24)$$

$$\mathcal{Z}_n(x, z, x_0, y_0, z_0) = \mathcal{Z}_{n,1} + \mathcal{Z}_{n,2}, \qquad (3.25)$$

292 and

$$\mathcal{Z}_{n,1} = \frac{1}{4\pi b}\left\{\delta_{n0}\left[\ln\left(\frac{r}{H}\right) + \ln\left(\frac{r'}{H}\right)\right] - 2(1 - \delta_{n0})\left[\mathcal{K}_0(\sigma_n r) + \mathcal{K}_0(\sigma_n r')\right]\right\}\cos \sigma_n(y_0 + b),$$
$$(3.26a)$$

$$\mathcal{Z}_{n,2} = \frac{\rho U}{2\pi b} \times$$
$$\int_{\mathscr{L}} \sum_{m=0}^{+\infty} \frac{k\mu_{n,m} \cosh K_m(z_0 + H) \cos \sigma_m(y_0 + b)\left[\cosh K_n(z + H)e^{\mathrm{i}k(x-x_0)} - \delta_{n0}\right]}{(1 + \delta_{m0})|\mathcal{A}|\Delta_m K_n \sinh K_n H \cosh K_m H} dk,$$
$$(3.26b)$$

296 where

$$\mu_{n,m} = \sum_{j=0}^{3} \beta_{n,j}c'_{m,j} + \delta_{m0}|\mathcal{A}|Uk\left(\frac{d_n^{(4)}}{24} + \frac{(1 - \delta_{n0})\gamma_n}{\sigma_n^4}\right)$$
$$+ \delta_{nm}|\mathcal{A}|\left[\frac{Uk(1 - \delta_{n0})}{\sigma_n^4} - \frac{\Delta_n(1 + e^{-2K_n H})}{2\rho Uk}\right]. \qquad (3.27)$$

298   It should be mentioned that a constant term is respectively added to $\mathcal{Z}_{n,1}$ and $\mathcal{Z}_{n,2}$ in
299 (3.26) to remove the high-order singularity at $k = 0$, which will not affect the results as all
300 the equations for G involve only its spatial derivatives. The term $\mathcal{Z}_{n,1}$ is obtained based on
301 the derivation in Li *et al.* (2020b). There will be singularities in $\mathcal{Z}_{n,2}$ when $|\mathcal{A}|(k) = 0$.
302 Because $|\mathcal{A}|(k)$ is an even function, all its real roots can be represented by $\pm k_s$ ($s = 1...S$),

303 with $k_s > 0$. In the case of Ren *et al.* (2020) for wave propagation in the channel, each k_s
304 corresponds to the dispersion relationship between the wave frequency and wave number.
305 Here mathematically each k_s corresponds to a singularity in the integrand of the inverse
306 Fourier transform. Physically, it corresponds to each wave generated by the source in the
307 channel. The number of singularities can be more than one, and the value of S depends on
308 the current speed U when other parameters are fixed, which will be discussed in detail later.
309 The way to treat each singularity will depend on the group velocity of its corresponding
310 wave. The wave will be at upstream ($x = +\infty$) or downstream ($x = -\infty$) if its group velocity
311 is larger or smaller than U respectively. Based on this, the integration route $\mathscr{L}$ in $\mathcal{Z}_{n,2}$ from
312 $-\infty$ to $+\infty$ can be defined as follows. We may consider the integration of $f(k)e^{ikx}/(k - k_s)$
313 along the path $\mathscr{L}$. This can be split into the principle integration and a contribution from the
314 pole. If the group velocity of the wave component k_s is larger (smaller) than U, $\mathscr{L}$ passes
315 over (under) the singularities at $\pm k_s$. Thus, the contribution from the pole at $k = k_s$ will be
316 $-i\pi f(k_s)e^{ik_s x}$ or $+i\pi f(k_s)e^{ik_s x}$. If we use Wehausen & Laitone (1960)

$$317 \qquad \lim_{|x| \to +\infty} \text{P.V.} \int_{-\infty}^{+\infty} \frac{f(k)}{k - k_s} e^{ikx} dk = \text{sgn}(x) i\pi f(k_s) e^{ik_s x}, \qquad (3.28)$$

318 in the integral in $\mathcal{Z}_{n,2}$, we can find that the radiation condition (2.12) is satisfied.
319   It may be of interest to see that the Green function is symmetric about source and filed
320 points, or $G(x, y, z, x_0, y_0, z_0) = G(x_0, y_0, z_0, x, y, z)$, which is shown in appendix B.

321   3.2. *Multipole expansion for the horizontal circular cylinder*

322   The Green function derived above can be used to convert the governing equation to an
323 integral equation over the surface of a body with arbitrary shape. For some special geometries,
324 such as a sphere, the solution may be found through expansion in terms of the multipole
325 obtained through differentiating the Green function with respect to the position of the source
326 (see example Wu (1998*b*)). For a horizontal circular cylinder, the potential can be expanded
327 into the cosine series as used for G. The governing Laplace equation in (x, y, z) then becomes
328 the modified Helmholtz equation in (x, z) for a circular section. Subsequently, the solution
329 of the modified Helmholtz equation can be obtained from a two-dimensional multipole
330 expansion. To construct that, we may apply a source distribution $\varsigma(y_0)$ along the centre line of
331 the cylinder. This is then expanded into the cosine series, or $\varsigma(y_0) = \sum_{n=0}^{+\infty} \mathcal{V}_n \cos \sigma_n(y_0 + b)$.
332 It will create the following potential

$$333 \qquad \varphi = \sum_{n=0}^{+\infty} \mathcal{V}_n \int_{-b}^{b} G \cos \sigma_n(y_0 + b) dy_0, \qquad (3.29)$$

334 where G is the Green function derived in the previous section. Substituting (3.24) into (3.29),
335 we obtain

$$336 \qquad \varphi = \sum_{n=0}^{+\infty} \varphi_n \cos \sigma_n (y + b), \qquad (3.30)$$

337 where

$$338 \qquad \varphi_n = \varphi_{n,1} + \varphi_{n,2}, \qquad (3.31)$$

339 with

$$340 \qquad \varphi_{n,1} = \frac{\mathcal{V}_n}{2\pi} \left\{ \delta_{n0} \left[\ln\left(\frac{r}{H}\right) + \ln\left(\frac{r'}{H}\right) \right] - (1 - \delta_{n0}) \left[\mathscr{K}_0(\sigma_n r) + \mathscr{K}_0(\sigma_n r') \right] \right\}, \qquad (3.32a)$$

$$\varphi_{n,2} = \frac{\rho U}{2\pi} \int_{\mathscr{L}} \sum_{n'=0}^{+\infty} \frac{\mathcal{V}_{n'}\mu_{n,n'}k \cosh K_{n'}(z_0 + H) \left[\cosh K_n(z + H)e^{\mathrm{i}k(x-x_0)} - \delta_{n0}\right]}{|\mathcal{A}|\Delta_{n'}K_n \sinh K_n H \cosh K_{n'} H} dk.$$

$$(3.32b)$$

We may use the operator

$$(D_\pm)^m = -\frac{1}{2^{m-1}(m-1)!}\left(\frac{\partial}{\partial z_0} \pm \mathrm{i}\frac{\partial}{\partial x_0}\right)^m.$$

$$(3.33)$$

This gives (Linton & McIver 2001)

$$(D_\pm)^m \ln r = \frac{e^{\pm \mathrm{i}m\theta}}{r^m},$$

$$(3.34a)$$

$$(D_\pm)^m \mathcal{K}_0(\sigma_n r) = \frac{(-1)^m \sigma_n^m}{2^{m-1}(m-1)!} e^{\pm \mathrm{i}m\theta} \mathcal{K}_m(\sigma_n r),$$

$$(3.34b)$$

where $z - z_0 = r\cos\theta$ and $x - x_0 = r\sin\theta$. As mentioned in Li *et al.* (2019), because φ is a real function, we may apply only the operator $(D_+)^m$. Using

$$(D_+)^m e^{\pm K_n z_0 \pm \mathrm{i}k x_0} = -\frac{(\pm 1)^m (K_n - k)^m}{2^{m-1}(m-1)!}e^{\pm K_n z_0 \pm \mathrm{i}k x_0},$$

$$(3.35a)$$

$$(D_+)^m e^{\pm K_n z_0 \mp \mathrm{i}k x_0} = -\frac{(\pm 1)^m (K_n + k)^m}{2^{m-1}(m-1)!}e^{\pm K_n z_0 \mp \mathrm{i}k x_0},$$

$$(3.35b)$$

as weel as (3.34), the velocity potential of the multipole can be expressed as

$$(\varphi_+)^m = (D_+)^m \varphi = \sum_{n=0}^{+\infty} (\varphi_+)_n^m \cos\sigma_n(y + b),$$

$$(3.36)$$

$$(\varphi_+)_n^m = (\varphi_+)_{n,1}^m + (\varphi_+)_{n,2}^m + (\varphi_+)_{n,3}^m,$$

$$(3.37)$$

where $(\varphi_+)_{n,1}^m + (\varphi_+)_{n,2}^m = (D_+)^m \varphi_{n,1}$, $(\varphi_+)_{n,3}^m = (D_+)^m \varphi_{n,2}$ and can be obtained as

$$(\varphi_+)_{n,1}^m = \frac{\mathcal{V}_n}{2\pi}\left[\delta_{n0}\frac{e^{\mathrm{i}m\theta}}{r^m} - (1 - \delta_{n0})\frac{(-1)^m \sigma_n^m}{2^{m-1}(m-1)!}e^{\mathrm{i}m\theta}\mathcal{K}_m(\sigma_n r)\right],$$

$$(3.38a)$$

$$(\varphi_+)_{n,2}^m = \frac{(-1)^m \mathcal{V}_n}{2^{m+1}(m-1)!\pi}\int_{-\infty}^{+\infty} \frac{(K_n - k)^m e^{-K_n(z+z_0+2H)+\mathrm{i}k(x-x_0)}}{K_n} dk,$$

$$(3.38b)$$

$$(\varphi_+)_{n,3}^m = \frac{-\rho U}{2^{m+1}(m-1)!\pi}\int_{\mathscr{L}} \sum_{n'=0}^{+\infty} \frac{\mathcal{V}_{n'}\mu_{n,n'}k\cosh K_n(z+H)E_{n',m}(k,z_0)e^{\mathrm{i}k(x-x_0)}}{|\mathcal{A}|\Delta_{n'}K_n \sinh K_n H \cosh K_{n'} H} dk,$$

$$(3.38c)$$

with

$$E_{n',m}(k, z_0) = (K_{n'} + k)^m e^{K_{n'}(z_0+H)} + (-1)^m (K_{n'} - k)^m e^{-K_{n'}(z_0+H)}.$$

$$(3.39)$$

The potential ϕ due to the cylinder then can be written in a multipole expansion form as

$$\phi = \mathrm{Re}\left\{\sum_{m=1}^{+\infty} r_0^m g_m(\varphi_+)^m\right\}.$$

$$(3.40)$$

It then satisfies all the boundary conditions met by the Green function and the only remaining

369 one is that on the cylinder surface. To satisfy the body surface boundary condition, we may
370 write the potential in the polar coordinate system. Using Abramowitz & Stegun (1970)

371
$$
\left.\begin{aligned}
e^{K_n(z-z_0)\pm ik(x-x_0)} &= \sum_{m=0}^{+\infty} T_{n,m}(r)\left[A_{n,m}^{\pm}(k)e^{im\theta} + A_{n,m}^{\mp}(k)e^{-im\theta}\right] \\
e^{-K_n(z-z_0)\pm ik(x-x_0)} &= \sum_{m=0}^{+\infty} (-1)^m T_{n,m}(r)\left[A_{n,m}^{\mp}(k)e^{im\theta} + A_{n,m}^{\pm}(k)e^{-im\theta}\right]
\end{aligned}\right\},
\tag{3.41}
$$

372 where

373
$$
\left.\begin{aligned}
A_{n,m}^{+}(k) &= \delta_{n0}k^m + (1-\delta_{n0})\left(\frac{K_n+k}{\sigma_n}\right)^m \\
A_{n,m}^{-}(k) &= (1-\delta_{n0})(1-\delta_{m0})\left(\frac{\sigma_n}{K_n+k}\right)^m \\
T_{n,m}(r) &= \delta_{n0}\frac{r^m}{m!} + (1-\delta_{n0})\mathscr{I}_m(\sigma_n r)
\end{aligned}\right\},
\tag{3.42}
$$

374 and $\mathscr{I}_m$ denotes the mth-order modified Bessel function of first kind, we have

375
$$
\phi = \mathrm{Re}\left\{\sum_{n=0}^{+\infty}\sum_{m=0}^{+\infty}\begin{bmatrix} Q_{n,m}f_{n,m}e^{im\theta} + T_{n,m}\sum_{m'=1}^{+\infty} f_{n,m'}\left(C_{n,m,m'}^{+}e^{im\theta} + C_{n,m,m'}^{-}e^{-im\theta}\right) \\ + T_{n,m}\sum_{n'=0}^{+\infty}\sum_{m'=1}^{+\infty} f_{n',m'}\left(\mathcal{D}_{n,n',m,m'}^{+}e^{im\theta} + \mathcal{D}_{n,n',m,m'}^{-}e^{-im\theta}\right) \end{bmatrix}\right.
$$
$$
\left. \times \cos\sigma_n(y+b)\right\},
\tag{3.43}
$$

376 where

377
$$
Q_{n,m}(r) = \frac{(1-\delta_{m0})}{2\pi}\left[\delta_{n0}\left(\frac{r_0}{r}\right)^m - \frac{(1-\delta_{n0})(-\sigma_n r_0)^m}{2^{m-1}(m-1)!}\mathscr{K}_m(\sigma_n r)\right],
\tag{3.44a}
$$

378

379
$$
C_{n,m,m'}^{\pm} = \frac{(-1)^{m+m'}r_0^{m'}}{2^{m'+1}(m'-1)!\pi}\int_{-\infty}^{+\infty}\frac{(K_n-k)^{m'}e^{-2K_n(z_0+H)}A_{n,m}^{\mp}}{K_n}dk,
\tag{3.44b}
$$

380

381
$$
\mathcal{D}_{n,n',m,m'}^{\pm} = \frac{-\rho U r_0^{m'}}{2^{m'+2}(m'-1)!\pi}\int_{\mathscr{L}}\frac{\mu_{n,n'}k\left[e^{K_n(z_0+H)}A_{n,m}^{\pm} + (-1)^m e^{-K_n(z_0+H)}A_{n,m}^{\mp}\right]E_{n',m'}}{\Delta_{n'}|\mathcal{A}|K_n\sinh K_n H\cosh K_{n'}H}dk.
\tag{3.44c}
$$

382 It should be mentioned here that a new unknown coefficient $f_{n,m}$ is defined as $f_{n,m} = \mathcal{V}_n g_m$.
383 The impermeable condition on the body surface in (2.8) gives

384
$$
Q_{n,m}'(r_0)f_{n,m} + T_{n,m}'(r_0)\sum_{m'=1}^{+\infty}\left(f_{n,m'}C_{n,m,m'}^{+} + \bar{f}_{n,m'}\bar{C}_{n,m,m'}^{-}\right)
$$
$$
+ T_{n,m}'(r_0)\sum_{n'=0}^{+\infty}\sum_{m'=1}^{+\infty}\left(f_{n',m'}\mathcal{D}_{n,n',n,m'}^{+} + \bar{f}_{n',m'}\bar{\mathcal{D}}_{n,n',m,m'}^{-}\right) = -\mathrm{i}\delta_{n0}\delta_{m1}U,
\tag{3.45}
$$

385 where $n = 0, 1, 2...$ and $m = 1, 2, 3...$ $Q_{n,m}'$ ($T_{n,m}'$) represents the derivative of $Q_{n,m}$ ($T_{n,m}$)

386 with respect to r, which can be obtained as

$$
\left.
\begin{aligned}
Q'_{n,m}(r) &= \frac{(1 - \delta_{m0})}{2\pi} \left[-\delta_{n0} m \frac{r_0^m}{r^{m+1}} + \frac{(1 - \delta_{n0})(-\sigma_n r_0)^{m+1}}{2^{m-1}(m-1)! r_0} \mathscr{K}'_m(\sigma_n r) \right] \\
T'_{n,m}(r) &= \delta_{n0} \frac{r^{m-1}}{(m-1)!} + (1 - \delta_{n0}) \sigma_n \mathscr{I}'_m(\sigma_n r)
\end{aligned}
\right\} .
\tag{3.46}
$$

388 After (3.45) is solved, ϕ can then be obtained.

3.3. *Hydrodynamic forces*

390 Once the potential is found, the lift F_L and resistance F_R on the cylinder can be calculated
391 through the integration of hydrodynamic pressure over the body surface. Thus, we have:

$$
-\mathrm{i}F_R + F_L = -\iint_{S_B} p e^{\mathrm{i}\theta} dS.
\tag{3.47}
$$

393 The pressure p can be obtained by the Bernoulli equation

$$
p = -\frac{1}{2}\rho \nabla(\phi - Ux) \cdot \nabla(\phi - Ux).
\tag{3.48}
$$

395 We may notice that the product term is kept here, as it may be small on the ice sheet but may
396 not be on the body surface. When determining the gradient term in (3.48) in the cylindrical
397 coordinate system, we may substitute (3.45) into (3.43) and have

$$
\left.
\begin{aligned}
\frac{\partial(\phi - Ux)}{\partial r}\bigg|_{r=r_0} &= 0 \\
\frac{\partial(\phi - Ux)}{\partial \theta}\bigg|_{r=r_0} &= \mathrm{Re}\left\{ \sum_{n=0}^{+\infty} \sum_{m=0}^{+\infty} \mathrm{i}m\psi_{n,m} e^{\mathrm{i}m\theta} \cos \sigma_n(y+b) \right\} \\
\frac{\partial(\phi - Ux)}{\partial y}\bigg|_{r=r_0} &= -\mathrm{Re}\left\{ \sum_{n=0}^{+\infty} \sum_{m=0}^{+\infty} \sigma_n\psi_{n,m} e^{\mathrm{i}m\theta} \sin \sigma_n(y+b) \right\}
\end{aligned}
\right\} ,
\tag{3.49}
$$

399 where

$$
\psi_{n,m} = f_{n,m}\left[Q_{n,m}(r_0) - Q'_{n,m}(r_0)\frac{T_{n,m}(r_0)}{T'_{n,m}(r_0)} \right].
\tag{3.50}
$$

401 Substituting (3.48) and (3.49) into (3.47), we obtain

$$
-\mathrm{i}F_R + F_L = \frac{\pi\rho b}{2r_0} \sum_{n=0}^{+\infty} \sum_{m=0}^{+\infty} \left[(1 + \delta_{n0})m(m+1) + (1 - \delta_{n0})\sigma_n^2 r_0^2 \right] \psi_{n,m}\bar{\psi}_{n,m+1}.
\tag{3.51}
$$

403 Similar to that in Wu (1995), the resistance can be also obtained by far-field integral, which
404 is shown in appendix C.

3.4. *Deflection of the ice sheet*

406 We may use (2.7) to obtain the expression of η, and this gives

$$
\eta(x, y) = -\frac{1}{U} \int \frac{\partial\phi}{\partial z} dx + C(y),
\tag{3.52}
$$

408 Substituting (3.36)~(3.40) into (3.52), we have

$$
\eta = \mathrm{Im}\left\{ \sum_{m=1}^{+\infty} \sum_{n=0}^{+\infty} r_0^m \eta_{n,m} \cos \sigma_n(y+b) \right\} + C(y),
\tag{3.53}
$$

$$\eta_{n,m} = \eta_{n,m}^{(1)} + \eta_{n,m}^{(2)} + \eta_{n,m}^{(3)}, \tag{3.54}$$

where

$$\eta_{n,m}^{(1)} = \frac{f_{n,m}}{2^{m+1}(m-1)!\pi U} \int_{-\infty}^{+\infty} \frac{(K_n + k)^m e^{K_n z_0 + \mathrm{i}k(x-x_0)}}{k} dk, \tag{3.55a}$$

$$\eta_{n,m}^{(1)} = \frac{(-1)^m f_{n,m}}{2^{m+1}(m-1)!\pi U} \int_{-\infty}^{+\infty} \frac{(K_n - k)^m e^{-K_n(z_0 + 2H) + \mathrm{i}k(x-x_0)}}{k} dk, \tag{3.55b}$$

$$\eta_{n,m}^{(3)} = \frac{\rho}{2^{m+1}(m-1)!\pi} \int_{\mathscr{L}} \sum_{n'=0}^{+\infty} \frac{f_{n',m}\mu_{n,n'} E_{n',m}(k, z_0) e^{\mathrm{i}k(x-x_0)}}{\Delta_{n'} |\mathcal{A}| \cosh K_{n'} H} dk. \tag{3.55c}$$

$C(y)$ in (3.52) is the integration constant. As $C(y)$ is not function of x, we may determine it at $x \to +\infty$. Based on (3.36)~(3.40) and (3.53)~(3.55), the asymptotic expressions of ϕ and η at $x \to +\infty$ can be written as

$$\phi = \mathrm{Re} \left\{ \sum_{j=1}^{S} \phi^{(j)}(y, z) e^{-\mathrm{i}k_j x} \right\} + \mathrm{sgn}(x)\phi^{(0)}(y, z), \tag{3.56}$$

$$\eta = \frac{1}{U}\mathrm{Re} \left\{ \sum_{j=1}^{S} \frac{1}{\mathrm{i}k_j} \frac{\partial \phi^{(j)}(y, 0)}{\partial z} e^{-\mathrm{i}k_j x} \right\} + C(y), \tag{3.57}$$

where $\phi^{(0)}$ is due to the singularity of the integrand at $k = 0$ and is related to the 'blockage parameter' (Mei & Chen 1976). It should be noted that the summation in (3.56) and (3.57) should include only those terms with group velocity larger than U. It can be shown $\partial\phi^{(0)}/\partial z = 0$ on $z = 0$ and therefore it does not contribute to η. We may combine (2.6) and (2.7) to eliminate η, and then use (3.56) in the result. We have

$$\left[L\left(k_j^4 - 2k_j^2 \frac{\partial^2}{\partial y^2} + \frac{\partial^4}{\partial y^4} \right) + \rho g \right] \frac{\partial \phi^{(j)}}{\partial z} - \rho U^2 k_j^2 \phi^{(j)} = 0, \; z = 0, \; x \to +\infty, \; j = 1 \sim S. \tag{3.58}$$

Substituting (3.56) and (3.57) into (2.6), and using (3.58), we obtain

$$L\frac{d^4 C}{dy^4} + \rho g C = 0. \tag{3.59}$$

The boundary conditions of C can be established by substituting (3.57) into (2.11) which is satisfied by the first term on the right-hand side of (3.57). This gives at $y = \pm b$

$$\left. \begin{array}{lll} C = 0, & C_y = 0, & \text{Clamped edge} \\ C = 0, & C_{yy} = 0, & \text{Simply supported edge} \\ C_{yy} = 0, & C_{yyy} = 0, & \text{Free edge} \end{array} \right\}. \tag{3.60}$$

It can be found that $C(y) = 0$ under any of these edge conditions.

3.5. *Numerical procedure*

Although the expression for the potential has been written explicitly, some of the computations still have to be performed numerically. Taking into account the integrand decays exponentially, the integration for k from $-\infty$ to $+\infty$ is truncated at a sufficiently large

439   value K_T and treated as

$$\text{P.V.} \int_{-\infty}^{+\infty} F(k)dk = \text{P.V.} \int_{0}^{+\infty} [F(k) + F(-k)]\, dk \approx \text{P.V.} \int_{0}^{K_T} [F(k) + F(-k)]\, dk,$$

440   (3.61)

441   P.V. indicates the Cauchy principal value. The range $(0, K_T)$ is divided into many small steps
442   and Gaussian method is used in each step for integration. To deal with multiple singularities
443   in the integrand, the following numerical procedures are applied. Assume that $F(k)$ contains
444   n first-order singularities in $k \in (0, +\infty)$. We may write

$$F(k) = \frac{G(k)}{\prod_{i=1}^{n}(k - k_i)} = G(k) \sum_{i=1}^{n} \frac{1}{\prod_{j=1(j \neq i)}^{n}(k_i - k_j)} \times \frac{1}{k - k_i}, \qquad (3.62)$$

446   Its Cauchy principal value can be calculated through

$$\text{P.V.} \int_{0}^{+\infty} F(k)dk = \sum_{i=1}^{n} \frac{1}{\prod_{j=1(j \neq i)}^{n}(k_i - k_j)} \left[\int_{0}^{2k_i} \frac{G(k) - G(k_i)}{k - k_i} dk + \int_{2k_i}^{+\infty} \frac{G(k)}{k - k_i} dk \right],$$

447   (3.63)

448   where $G(k)$ can be calculated by

$$\left.\begin{array}{ll} G(k) = F(k) \displaystyle\prod_{i=1}^{n}(k - k_i), & k \neq k_i \\[4mm] G(k_i) = \displaystyle\prod_{j=1(j \neq i)}^{n}(k_i - k_j) \lim_{k \to k_i}(k - k_i)F(k), & i = 1 \sim n \end{array}\right\}. \qquad (3.64)$$

450   By doing that, all the singularity effects are eliminated. Although the original one integral is
451   split into n integrals, it is still more computationally efficient, as the integration step Δk can
452   be appropriately chosen for each integral. For a single integral of $F(k)$, Δk has to be very
453   small, especially when some of the singularities are very close to each other.
454   When determining the residue at the singularities caused by $|\mathcal{A}|(k_s) = 0$, the value of
455    $|\mathcal{A}|'(k_s)$ needs to be calculated numerically. Here we adopt the method proposed by Li *et al.*
456   (2020*b*). Assuming $f(k)/(k - k_s) = g(k)/|\mathcal{A}|(k) = P(k)$, we have

$$f(k_s) = \frac{g(k_s)}{|\mathcal{A}|'(k_s)} = \lim_{k \to k_s}(k - k_s)P(k) \approx \frac{P(k_s + \Delta k) - P(k_s - \Delta k)}{2}\Delta k. \qquad (3.65)$$

4. Numerical Results

459   The typical values of the physical parameters of the ice sheet and the channel are chosen
460   as below

$$\left.\begin{array}{l} \rho_i = 917 \text{ kg m}^{-3}, \;\; h_i = 0.15 \text{ m}, \;\; E = 4.2 \times 10^9 \text{ N m}^{-2}, \;\; \nu = 0.3 \\[2mm] \rho = 1000 \text{ kg m}^{-3}, \;\; g = 9.81 \text{ m s}^{-2}, \;\; H = 10\text{m}, \;\; b = 20\text{m}, \;\; r_0 = 1 \text{ m} \end{array}\right\}. \qquad (4.1)$$

462   The calculations undertaken below are based on these parameters unless otherwise specified.
463   All the numerical results are presented in the dimensionless form, based on a characteristic
464   length, the fluid density ρ and acceleration g due to gravity. The depth-based Froude number
465   is defined as $Fn = U/\sqrt{gH}$.

4.1. *Analysis of the dispersion relationship of an ice-covered channel*

467   As discussed after (3.24), there are singularities in the integrand when $|\mathcal{A}|(k, U) =$
468    $|\mathcal{A}|(\hat{k}, Fn) = 0$ (where $\hat{k} = kH$), which are equivalent to the dispersion relationship
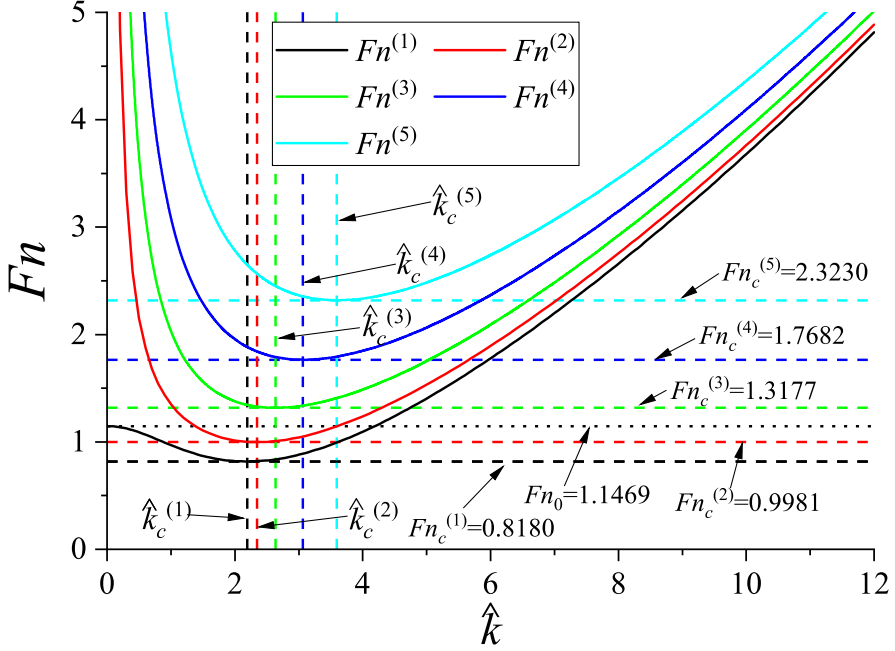
Figure 2: Purely positive solution of $|\mathcal{A}|(\hat{k}, Fn) = 0$ for clamped-clamped edges condition.

and correspond to the waves at infinity. Compared with the two-dimensional case of a homogeneous ice plate with infinite extent (Li *et al.* 2019), the dispersion relationship here is more complicated. The root Fn of the equation at each given $\hat{k}$ is not unique. In fact, there is an infinite number of solutions of Fn at a given $\hat{k}$, we denote this these solutions as $Fn^{(i)}$ ($i = 1, 2, 3...$), with $Fn^{(1)} < Fn^{(2)} < Fn^{(3)} < ....$ Similar to that in Khabakhpasheva *et al.* (2019), the curves $Fn^{(i)}$ against $\hat{k}$ are shown in figure 2. It can be seen that for each curve there is a minimum value at $\hat{k} = \hat{k}_c^{(i)}$, which can be called ith-order critical Froude number and be denoted by $Fn_c^{(i)}$. The value of each $Fn_c^{(i)}$ can be found in figure 2. When $Fn < Fn_c^{(1)}$, there will be no solution in $|\mathcal{A}|(\hat{k}, Fn) = 0$, or there will be no waves propagating to $x = \pm\infty$. When $Fn_c^{(1)} < Fn < Fn_c^{(2)}$, there will be two solutions in $|\mathcal{A}|(\hat{k}, Fn) = 0$. The ones corresponding to $\hat{k} < \hat{k}_c^{(1)}$ and $\hat{k} > \hat{k}_c^{(1)}$ will lead to waves at $x = -\infty$ and $x = +\infty$ respectively, because their group velocities are smaller and larger than U respectively, as in Li *et al.* (2019). In fact, the nondimensionalized group velocity $c_g^{(s)}$ can be obtained as

$$c_g^{(s)} = Fn(\hat{k}_s) + \hat{k}_s \frac{d}{d\hat{k}} Fn(\hat{k}_s), \qquad (4.2)$$

where $(\hat{k}_s, Fn(\hat{k}_s))$ is an intersection point of Fn with curve $\hat{k} - Fn^{(i)}$. It can be observed from figure 2 and (4.2) that when $\hat{k}_s < \hat{k}_c^{(i)}$ ($\hat{k}_s > \hat{k}_c^{(i)}$), the slope $dFn(\hat{k}_s)/d\hat{k} < 0$ ($dFn(\hat{k}_s)/d\hat{k} > 0$), and the group velocity $c_g^{(s)} < Fn(\hat{k}_s)$ ($c_g^{(s)} > Fn(\hat{k}_s)$) and wave will be at $x = -\infty$ ($x = +\infty$).

As Fn increases, it will reach the second critical point $Fn_c^{(2)}$. Beyond that, there will be two more solutions in $|\mathcal{A}|(\hat{k}, Fn) = 0$. This leads to two more waves and one each at $x = -\infty$ and $x = +\infty$. In general, when $Fn_c^{(i)} < Fn < Fn_c^{(i+1)}$, there will be $2i$ roots in $|\mathcal{A}|(\hat{k}, Fn) = 0$, and i waves at $x = -\infty$ and $x = +\infty$ respectively. However, the curve $Fn_c^{(1)}$ is different from
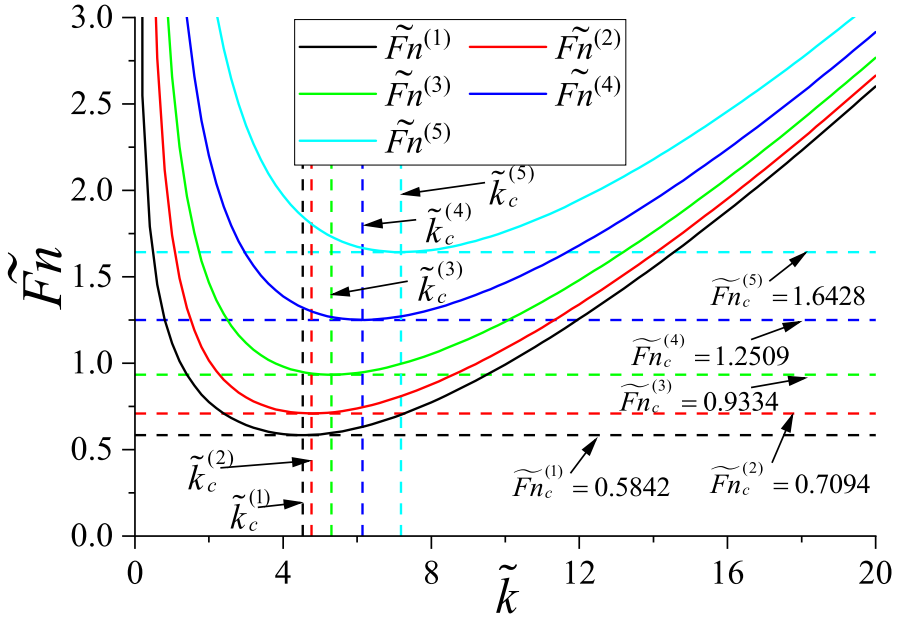
Figure 3: Purely positive solution of $|\mathcal{A}|(\widetilde{k}, \widetilde{Fn}) = 0$ for clamped-clamped edges at $H \to +\infty$.

491   others. When $\hat{k} \to 0$, we can see that $\lim_{\hat{k} \to 0} Fn^{(1)} = Fn_0$ while $\lim_{\hat{k} \to 0} Fn^{(i)} = +\infty$ ($i \geqslant 2$).
492   Therefore, when $Fn > Fn_0$, corresponding to curve $Fn^{(1)}$, there will be only one solution in
493   $|\mathcal{A}|(\hat{k}, Fn) = 0$, and there will be $2i - 1$ solutions when $Fn_c^{(i)} < Fn < Fn_c^{(i+1)}$.

494   As mentioned in Section 3.1, the symmetric and anti-symmetric transverse waves are
495   completely independent in the cases of symmetric edges. If we further write $|\mathcal{A}|$ as in
496   (A 10), it can be found that all the intersection points on curve $Fn^{(2i-1)}$ ($i \geqslant 1$) in figure 2
497   are solutions of $|\mathcal{A}^S|(\hat{k}, Fn) = 0$ and correspond to symmetric mode, while those on curve
498   $Fn^{(2i)}$ are solutions of $|\mathcal{A}^A|(\hat{k}, Fn) = 0$ and correspond to anti-symmetric mode.

499   In the two-dimensional case, there is only one critical Fn_c, below which there will be
500   no wave, and above which will be two waves at $x = -\infty$ and $x = +\infty$ respectively. When
501   $Fn > 1$, the wave at downstream region will disappear but the one at upstream region will
502   remain. Here when there is an infinite number of critical Froude number. $Fn_c^{(1)}$ is similar
503   to Fn_c in the two-dimensional case, below which there will be no wave. As Fn increases
504   and passes through each $Fn^{(i)}$ ($i = 1, 2, 3...$) each pair of waves will be created, with one
505   at downstream and the other at upstream regions. Fn_0 here corresponds to $Fn = 1$ in the
506   two-dimensional case. When $Fn > Fn_0$, the wave at $x = -\infty$ due to $Fn^{(1)}$ will disappear,
507   which is similar to the two-dimensional case. However, different from the two-dimensional
508   case, there will be still waves at downstream region.

509   The feature of wave in infinite water depth or $H \to +\infty$ is also investigated, other
510   parameters in (4.1) are kept the same. For the two-dimensional case, the critical value
511   $Fn = 1$ will disappear if $H \to +\infty$. There will always be two waves, with one each at
512   downstream and upstream regions respectively when the current speed is larger than the
513   critical value. Here, using $\lim_{H \to +\infty} \tanh K_n H = 1$, $\alpha_{n,j}$ in (3.17a) can be further expressed
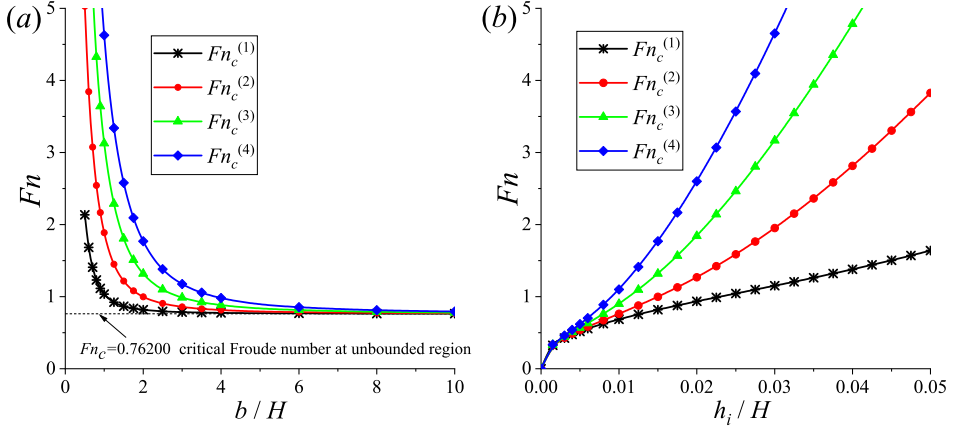
Figure 4: Critical Froude number under clamped-clamped edges condition. (*a*) $Fn_c^{(i)}$ ($i = 1 \sim 4$) at different channel widths; (*b*) $Fn_c^{(i)}$ ($i = 1 \sim 4$) at different ice sheet thickness.

514   as

$$\alpha_{n,j} = \frac{1}{\Delta_n^\infty} \left\{ \begin{array}{l} d_n^{(j)}[(\rho g + Lk^4)K_n - \rho k^2 U^2] \\ - 4k^2 L d_n^{(0)} K_n \delta_{2j} - 12k^2 L d_n^{(1)} K_n \delta_{3j} \end{array} \right\} + (1 - \delta_{n0}) \gamma_n^\infty \alpha_{0j}, \qquad (4.3)$$

516   where

$$\Delta_n^\infty = \left\{ \begin{array}{l} \delta_{n0} \left[-\left(\dfrac{\rho g + Lk^4}{24} d_n^{(4)} - k^2 L d_n^{(2)} + L \right) K_n + \dfrac{\rho k^2 U^2}{24} d_n^{(4)} \right] \\ + (1 - \delta_{n0}) \left[-\left(\dfrac{\rho g + Lk^4}{\sigma_n^4} + \dfrac{2k^2 L}{\sigma_n^2} + L \right) K_n + \dfrac{\rho k^2 U^2}{\sigma_n^4} \right] \end{array} \right\}, \qquad (4.4a)$$

$$\gamma_n^\infty = \frac{1}{\Delta_n^\infty} \left[\left(\frac{\rho g + Lk^4}{24} d_n^{(4)} - k^2 L d_n^{(2)} \right) K_n - \frac{\rho k^2 U^2}{24} d_n^{(4)} \right]. \qquad (4.4b)$$

520   If the half-width b is chosen as the characteristic length, two new parameters can be defined
521   as $\widetilde{Fn} = U/\sqrt{gb}$ & $\widetilde{k} = kb$. Substituting (4.3) into (A 2), the solution of $|\mathcal{A}|(k, U) = |\mathcal{A}|(\widetilde{k}, \widetilde{Fn}) = 0$ at $H \to +\infty$ can be obtained and shown in figure 3. Similar to $Fn_c^{(i)}$ in figure
523   2, the ith-order critical value at $\widetilde{k} = \widetilde{k}_c^{(i)}$ is defined as $\widetilde{Fn}_c^{(i)}$. It can be seen that the curve
524    $\widetilde{Fn}^{(1)}$ is different from $Fn^{(1)}$ in figure 2. When $\widetilde{k} \to 0$, we can find that $\lim_{\widetilde{k} \to 0} \widetilde{Fn}^{(1)} = +\infty$.
525   Therefore, there will always be $2i$ solutions in $|\mathcal{A}|(\widetilde{k}, \widetilde{Fn}) = 0$ when $\widetilde{Fn}_c^{(i)} < \widetilde{Fn} < \widetilde{Fn}_c^{(i+1)}$,
526   which leads to i waves at $x = -\infty$ and $x = +\infty$ respectively.
527   We may also investigate how the above results vary with the channel width b, ice sheet
528   thickness h_i and various edge constraints while other values in (4.1) remain unchanged. $Fn_c^{(i)}$
529   ($i = 1, 2, 3, 4$) at different b and h_i under clamped-clamped edges is shown in figure 4. It
530   can be seen from figure 4(*a*) that all the $Fn_c^{(i)}$ decrease when b increases, and they all tend
531   to the value of Fn_c without the tank wall, or the two-dimensional case (Li *et al.* 2019). In
532   other words, when b increases, the curves $Fn^{(i)}$ in figure 2 will gradually move towards each
533   other and approach the curve in the two-dimensional case. figure 4(*b*) shows that at $h_i = 0$
534   all the $Fn_c^{(i)} = 0$, which is expected as this is a free surface problem. As h_i increases, all
535   the $Fn_c^{(i)}$ increase. As h_i becomes very large or L is very large, the ice sheet becomes a
536   rigid plate and there will be no waves, which means $Fn_c^{(i)} \to +\infty$. In figures 5(*a*) and (*b*),
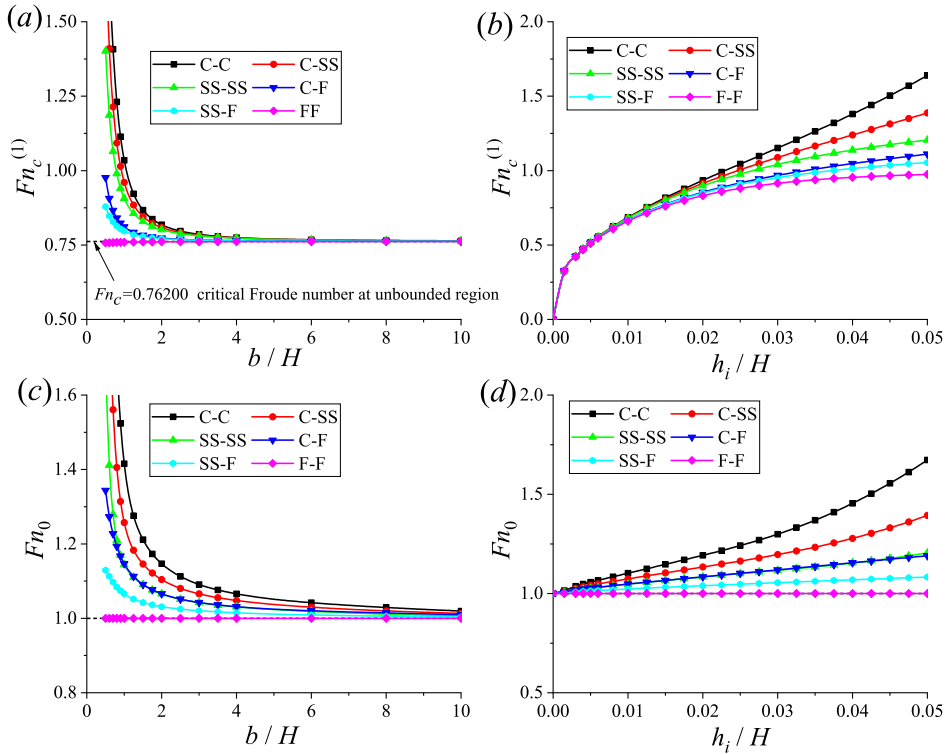
Figure 5: $Fn_c^{(1)}$ and Fn_0 under different edges conditions. (*a*) $Fn_c^{(1)}$ at different channel widths; (*b*) $Fn_c^{(1)}$ at different ice thickness; (*c*) Fn_0 at different channel widths; (*d*) Fn_0 at different ice thickness. The clamped edge is denoted by C, simply supported edge is by SS and the free edge is by F (The same below).

$Fn_c^{(1)}$ under other edges conditions show variation trends similar to that in figure 4, apart from the free-free one where $Fn_c^{(1)}$ increases slightly with b. Fn_0 versus with b and h_i are given in figures 5(*c*) and (*d*) respectively. It can be shown that under free-free condition, $Fn_0 = 1$, which can be confirmed by substituting $\hat{k} = 0$ and $Fn = 1$ in $|\mathcal{A}|(\hat{k}, Fn)$. This is the same as the two-dimensional case. Under other edges conditions Fn_0 is different from 1. It varies with b in a way similar to that of $Fn_c^{(1)}$. It can be observed that at sufficiently large b, $Fn_0 \to 1$, which is consistent with the two-dimensional case. Also $\lim_{h_i \to 0} Fn_0 = 1$, which is consistent with the free surface problem. Another interesting feature in figure 5 is when all the parameters are fixed, $Fn_c^{(1)}$ and Fn_0 increase in the following sequence: free-free, simply supported-free, clamped-free, simply supported-simply supported, clamped-simply supported and clamped-clamped.

4.2. *Deflection of the ice sheet due to an underwater source*

Numerical results are first given for the ice sheet deflection ξ induced by a submerged source. The quiescent water depth H is used as the characteristic length. ξ can be obtained directly by using inverse Fourier transformation

$$\xi = \frac{1}{2\pi} \int_{-\infty}^{+\infty} \hat{\xi} e^{\mathrm{i}kx} dk. \tag{4.5}$$
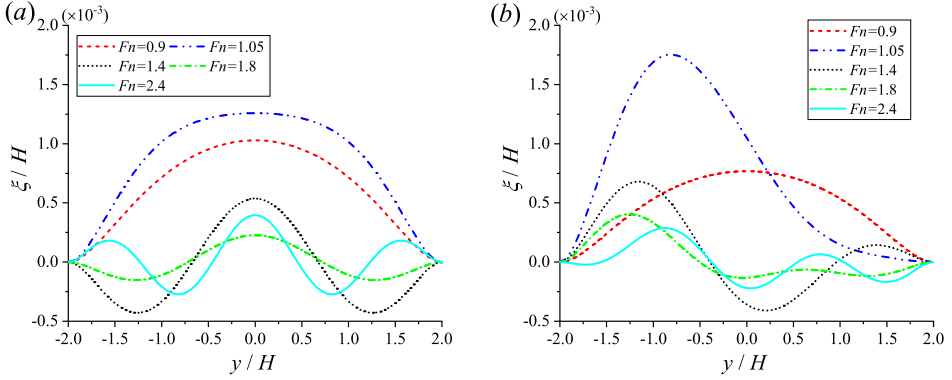
Figure 6: Ice sheet deflection ξ along $y-$axis due to a source when the ice sheet is under clamped-clamped edges condition. (a) $(x_0, y_0, z_0) = (0, 0, -H/5)$; (b) $(x_0, y_0, z_0) = (0, -b/2, -H/5)$. The Froude numbers in the figure are in the following order: $Fn_c^{(1)} = 0.8180 < 0.9 < Fn_c^{(2)} = 0.9981 < 1.05 < Fn_c^{(3)} = 1.3177 < 1.4 < Fn_c^{(4)} = 1.7682 < 1.8 < Fn_c^{(5)} = 2.3230 < 2.4 < Fn_c^{(6)} = 2.9600.$

553 Substituting (3.7) into (4.5) and using (3.24) $\sim$ (3.27), we have

$$554 \quad \xi = \frac{i\rho}{2\pi b} \int_{\mathscr{L}} \sum_{n=0}^{+\infty} \sum_{m=0}^{+\infty} \frac{\lambda_{n,m} \cosh K_m(z_0 + H)e^{ik(x-x_0)} \cos \sigma_n(y + b) \cos \sigma_m(y_0 + b)}{(1 + \delta_{m0})\Delta_m|\mathscr{A}| \cosh K_m H} dk, \quad (4.6)$$

555 where

$$556 \quad \lambda_{n,m} = \sum_{j=0}^{3} \beta_{n,j} c'_{m,j} + \delta_{m0}|\mathscr{A}|Uk\left(\frac{d_n^{(4)}}{24} + \frac{(1 - \delta_{n0})\gamma_n}{\sigma_n^4}\right) + \delta_{nm}(1 - \delta_{n0})\frac{Uk|\mathscr{A}|}{\sigma_n^4}. \quad (4.7)$$

557 It should be noted that the infinite series in (4.6) is truncated at $n = m = 15$ in the calculation,
558 and the results have been found to have converged.
559   The ice deflection along $y-$axis induced by a source at two different locations under
560 clamped-clamped edges are shown in figure 6. In figure 6(a), the source is located at
561 $(x_0, y_0, z_0) = (0, 0, -H/5)$. This corresponds to a symmetric case about $y = 0$, or only
562 waves correspond to even m in (4.6) will exist. As $x = 0$ and $x_0 = 0$, the principal integral of
563 ξ in (4.6) is zero. The remaining waves are those components which will propagate to $x = +\infty$
564 and $x = -\infty$ respectively. It can be seen from figure 6(a) that the wave profiles at $Fn = 0.9$ and
565 $Fn = 1.05$ are dominated by the first symmetric transverse mode (σ_2), and at $Fn = 1.4$ and
566 $Fn = 1.8$ the second symmetric mode (σ_4) become important, further at $Fn = 2.4$, the third
567 symmetric mode (σ_6) also becomes important. In general, when $Fn_c^{(2m-1)} < Fn < Fn_c^{(2m+1)}$
568 ($m \geqslant 1$), the contribution of the m-th symmetric mode (σ_{2m}) to the overall wave profile will
569 be significant. As $c_1 = c_3 = 0$ and $a_{2n-1} = b_{2n-1} = 0$ in (3.5) and (3.9), the singularities
570 corresponding to $|\mathscr{A}^A|(\hat{k}, Fn) = 0$ (see (A 6)) in the solution for these coefficients are no
571 longer relevant. Therefore, the curves of $Fn^{(2i)}(\hat{k})$ can be removed from figure 2 in such a
572 case. The transverse wave profiles with the source located at $(x_0, y_0, z_0) = (0, -b/2, -H/5)$
573 are shown in figure 6(b), which is an asymmetric case. In such a case, all the longitudinal
574 wave components of k_j ($j = 1 \sim S$) in (4.6) exist, and all the transverse waves of σ_m will
575 also exist. The overall transverse wave in this case is asymmetric.
576   The hydroelastic waves along the $x-$axis due to a source at $(x_0, y_0, z_0) = (0, 0, -H/5)$ are
577 given in figure 7. It can be seen from figure 7(a) that there is no wave propagating to $x = \pm\infty$
578 when $Fn < Fn_c^{(1)}$. The longitudinal wave profile is anti-symmetric about $x = x_0$, which can
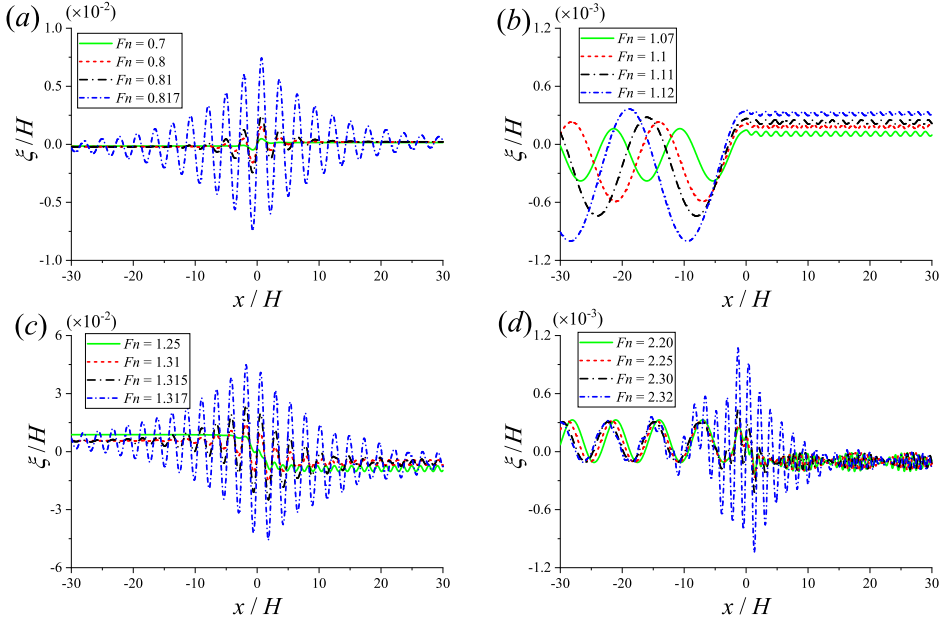
Figure 7: Ice sheet deflection ξ along x−axis due to a source located at $(x_0, y_0, z_0) = (0, 0, -H/5)$ when the ice sheet is under clamped-clamped edges condition. (a) $Fn < Fn_c^{(1)}$; (b) $Fn_c^{(1)} < Fn < Fn_0$; (c) $Fn_c^{(2)} < Fn < Fn_c^{(3)}$; (d) $Fn_c^{(4)} < Fn < Fn_c^{(5)}$. $Fn_c^{(1)} = 0.8180$, $Fn_c^{(2)} = 0.9981$, $Fn_c^{(3)} = 1.3177$, $Fn_c^{(4)} = 1.7682$, $Fn_c^{(5)} = 2.3230$, $Fn_0 = 1.1469$.
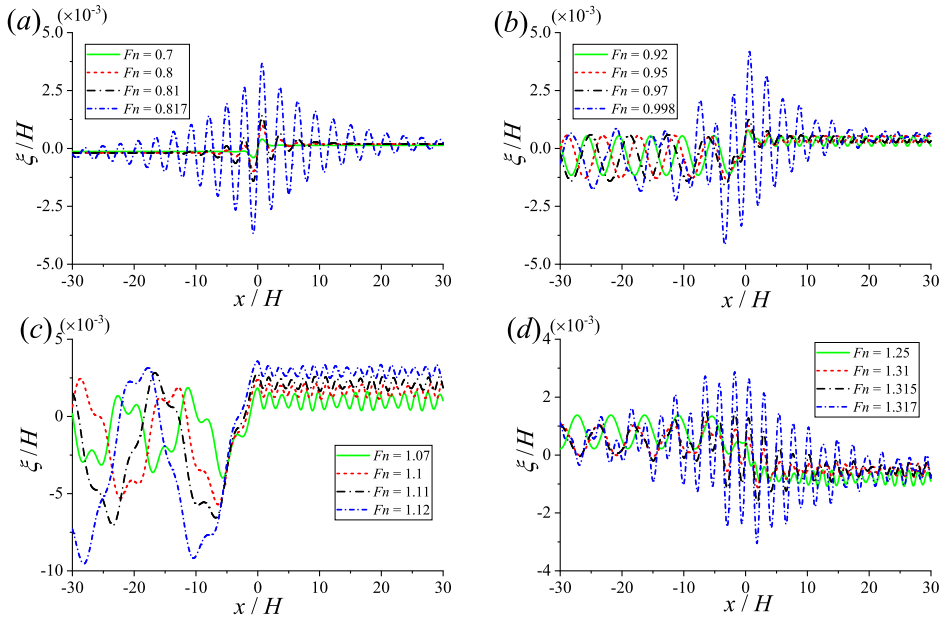

Figure 8: Ice sheet deflection ξ along $y = -b/2$ due to a source located at $(x_0, y_0, z_0) = (0, -b/2, -H/5)$ when the ice sheet is under clamped-clamped edges condition. (a) $Fn < Fn_c^{(1)}$; (b) $Fn_c^{(1)} < Fn < Fn_c^{(2)}$; (c) $Fn_c^{(2)} < Fn < Fn_0$; (d) $Fn_0 < Fn < Fn_c^{(3)}$. $Fn_c^{(1)} = 0.8180$, $Fn_c^{(2)} = 0.9981$, $Fn_c^{(3)} = 1.3177$, $Fn_0 = 1.1469$.

be confirmed by the sine function in the principal integral of (4.6). As Fn increases, it can
be seen that in figures 7(*a*), (*c*) and (*d*) that the wave elevation near $x = x_0$ is significantly
increased when Fn is near each of $Fn_c^{(i)}$ ($i = 1, 3, 5...$). When $Fn \to Fn_0$, the smaller
root of $Fn^{(1)}(\hat{k}) = Fn$ tends to zero, and the corresponding wavelength at $x = -\infty$ tends
to infinity, which can be observed from figure 7(*b*). Since waves corresponds the roots of
$Fn^{(2i)} = Fn$ will not appear in the symmetric case, there is no wave propagating to $x = -\infty$
when $Fn_0 < Fn < Fn_c^{(3)}$. As discussed in appendix B, due to the net mass outflow from
the source, or mathematically the singularity of function $\hat{\xi}$ at $k = 0$, opposite mean wave
elevations can be observed at $x \to +\infty$ and $x \to -\infty$, which are denoted by $\bar{\xi}_{+\infty}$ and $\bar{\xi}_{-\infty}$
respectively. It is also interesting to see that $\bar{\xi}_{+\infty} > 0$ ($\bar{\xi}_{-\infty} < 0$) when $Fn < Fn_0$, while
$\bar{\xi}_{+\infty} < 0$ ($\bar{\xi}_{-\infty} > 0$) when $Fn > Fn_0$. In figure 8, the ice sheet deflection along $y = -b/2$
generated by a source located at $(x_0, y_0, z_0) = (0, -b/2, -H/5)$ is plotted. Phenomena similar
to those in figure 7 may be also observed, apart from that waves corresponding to the roots
of $Fn^{(2i)} = Fn$ also appear. In fact, from figures 8(*c*) and (*d*), we can see clearly the wave
behind the source due to $Fn^{(2)}$ when $Fn > Fn_c^{(2)}$.

4.3. *Hydrodynamic forces on a submerged horizontal cylinder*

A submerged horizontal cylinder with its centre line located at $x_0 = 0$ and $z_0 = -H/5$ in
the current is considered next. The radius of the cylinder r_0 is employed as the characteristic
length. For the free surface problem, the two-dimensional steady solution may no longer be
possible within some ranges of the Froude number at a given submergence (Haussling &
Coleman 1979; Scullen & Tuck 1995; Semenov & Wu 2020). This is mainly because the
steady wave amplitude reaches its limit and may break, which is reflected by the fact the
velocity magnitude at the wave peak tends to zero (Semenov & Wu 2020). This can occur
when the submergence of the circular cylinder is chosen as $|z_0|/r_0 = 2$ for the free surface
flow. However, here the problem is quite different. On the one hand, the covering ice sheet
will obviously affect the behavior of the waves. More importantly, the case considered here
is a three-dimensional one. For clamped edges as an example, the wave elevation along the
edge is in fact zero. Indeed, it also has been found from the obtained numerical results that
the magnitude of the velocity on the far-field is always positive for the case considered apart
from that near the critical Froude numbers. This suggests that the linear model is valid apart
from when Froude number is near one of the critical values. At the critical value, the results
of the linear model become inaccurate while its prediction for the critical value itself may be
accurate. In such a case, nonlinearity and other effects may need to be taken into account.

To conduct numerical computations, the infinite series in (3.45) is truncated at $n' = N$ and
$m' = M$. A convergence test is then carried out for N and M through the hydrodynamic forces
on the cylinder when the ice sheet is under clamped-clamped edges condition. The far-field
formula (C 7) is also employed to check the resistance F_R obtained by the near field formula
(3.51). The convergence test results are shown in figure 9. An excellent agreement can be
seen between the results obtained by $N = 15$ & $M = 15$ and $N = 25$ & $M = 25$, which means
the convergence has been achieved. Therefore, $N = 15$ & $M = 15$ is applied in the following
calculation. We can also observe that the resistance calculated by (C 7) is graphically the
same as that from (3.51). It can be seen from figure 9(*a*) that $F_R = 0$ when $Fn < Fn_c^{(1)}$,
which is similar to the two-dimensional case considered by Li *et al.* (2019). As mentioned
above, there is no wave at infinity when $Fn < Fn_c^{(1)}$, which leads to that coefficients $Q_{n,m}$,
$C_{n,m,m'}^{\pm}$ and $\mathcal{D}_{n,n',m,m'}^{\pm}$ in (3.45) are all real, and correspondingly the solution $f_{n,m}$ should be
imaginary. Together with (3.50), $\psi_{n,m}$ is imaginary, then from (3.51), we have $F_R = 0$.

We then consider the resistance and lift under three different symmetric edge constraints.
The results are provided in figure 10. In figure 10(*a*). When the Froude number passes $Fn =$
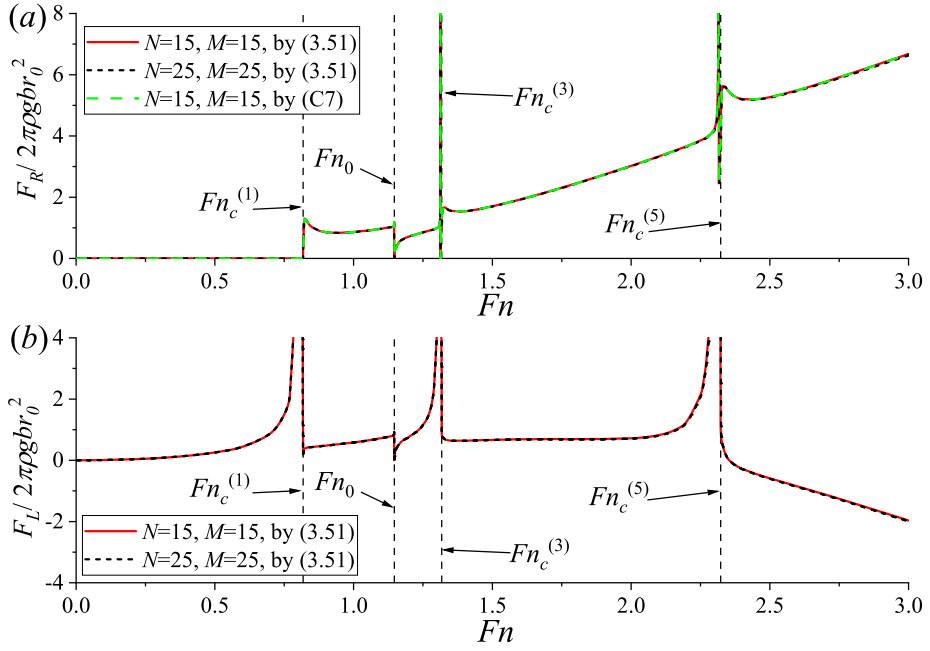
Figure 9: Convergence study for the hydrodynamic forces on the cylinder when the ice sheet is under clamped-clamped edge condition. (a) Resistance; (b) Lift.
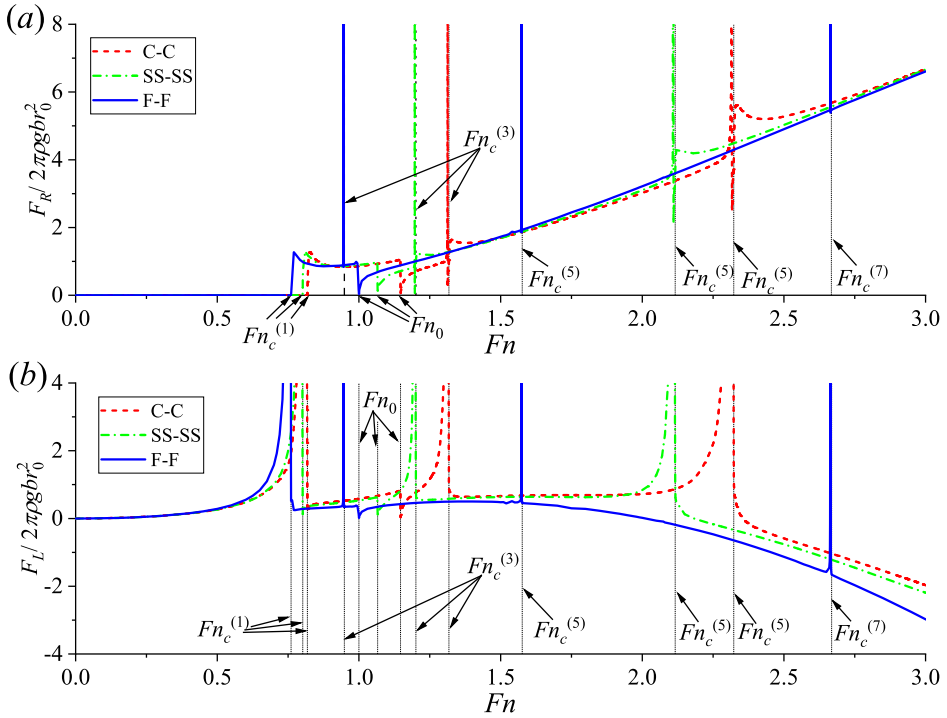

Figure 10: Hydrodynamic forces on the cylinder when the ice sheet is under symmetric edges conditions. (a) Resistance; (b) Lift.
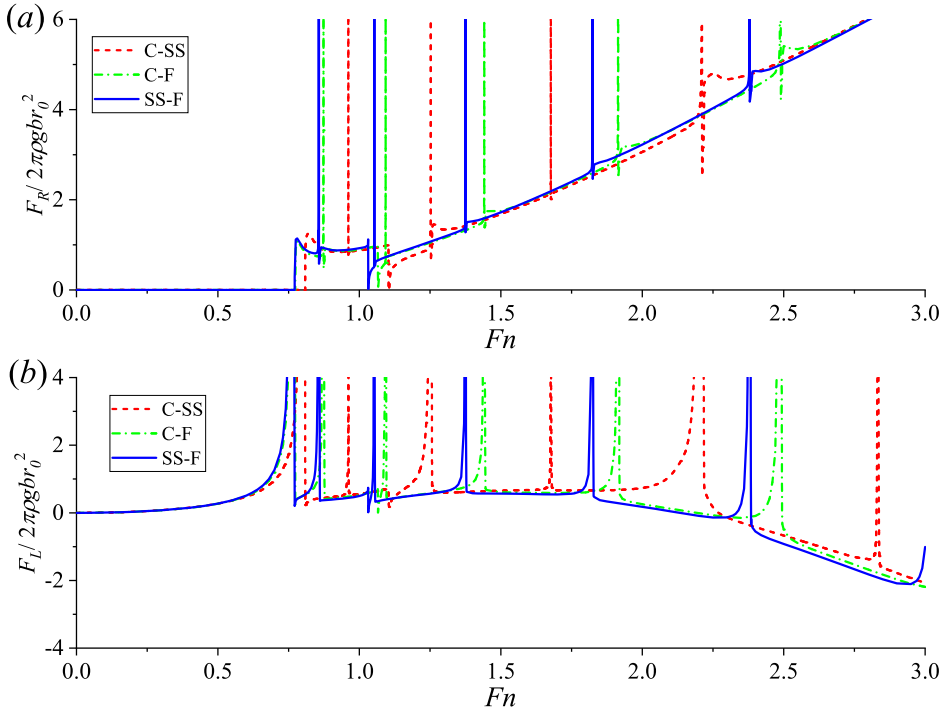
Figure 11: Hydrodynamic forces on the cylinder when the ice sheet is under asymmetric edges conditions. (*a*) Resistance; (*b*) Lift.

$Fn_c^{(i)}$ ($i \geqslant 1$) or Fn_0, the resistance changes rapidly. The number of the wave components at far-field will also change. In particular the resistance F_R is zero initially. When Fn passes $Fn = Fn_c^{(1)}$, F_R jumps up rapidly. As Fn passes Fn_0, F_R will have a sharp drop. These are similar to the behaviours of the resistance at $Fn = Fn_c$ and $Fn = 1$ in the two-dimensional case considered by Li *et al.* (2019). When Fn continues to increase and pass $Fn_c^{(2i-1)}$ ($i \geqslant 2$), F_R will first increase rapidly and then decrease rapidly, and return to almost original trajectory of the curve. In the two-dimensional case, critical values of $Fn_c^{(i)}$ ($i > 1$) do not exist. For the F_L given in figure 10(*b*), it is nonzero even at small Fn because the flow is not symmetric about $z = z_0$. The lift near $Fn_c^{(2i-1)}$ ($i \geqslant 1$) and Fn_0 have a behaviour similar to that of resistance. At large Fn the lift may become negative similar to the free surface problem (Wu & Eatock Taylor 1987). It is also interesting to see from figure 10 that the differences in F_R or F_L under various edge conditions are much more obvious in the region near $Fn_c^{(i)}$ and Fn_0. When Fn passes $Fn_c^{(2i-1)}$ ($i > 1$), we can see that the jump phenomena of F_L and F_R in the case of free-free edges are not as obvious as those of clamped-clamped and simply supported-simply supported edges. The variation of F_R and F_L against Fn under three asymmetric edges constraints are shown in figure 11. Behaviours similar to those in figure 10 may be observed. However, as mentioned in Section 4.2, in addition to $Fn_c^{(2i-1)}$, $Fn_c^{(2i)}$ will also affect the waves in these asymmetric cases about $y = 0$. As a result, more sudden changes can be observed in figure 11.

Computations are then carried out to investigate the effect of the channel width *b*. A comparison with the two-dimensional cases given in Fig. 4 of Li *et al.* (2019) is also conducted. It should be noted that apart from there are channel width *b* and edge conditions
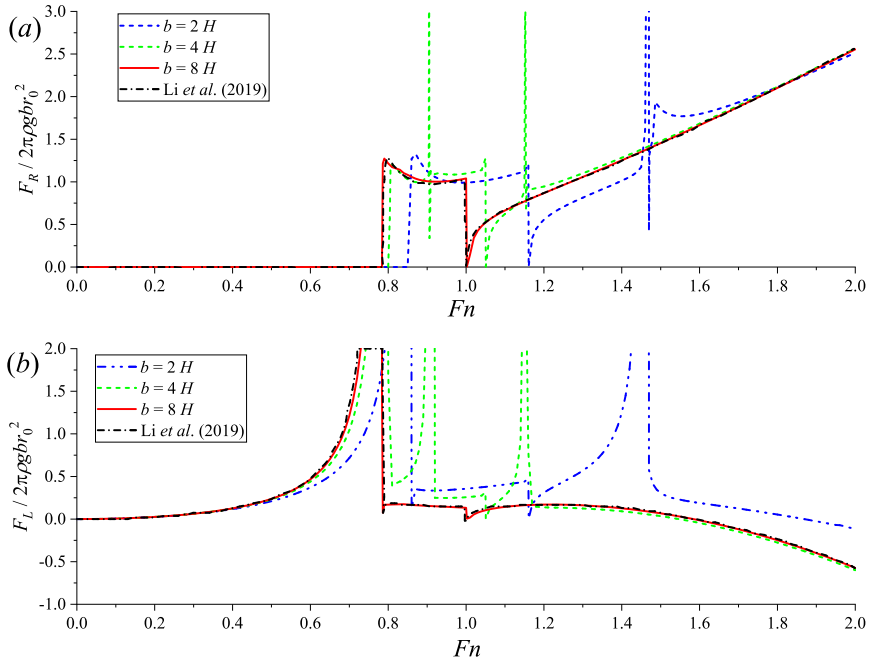
Figure 12: Hydrodynamic forces on the cylinder in an ice-covered channel with clamped - clamped edges at different channel widths. (*a*) Resistance; (*b*) Lift.
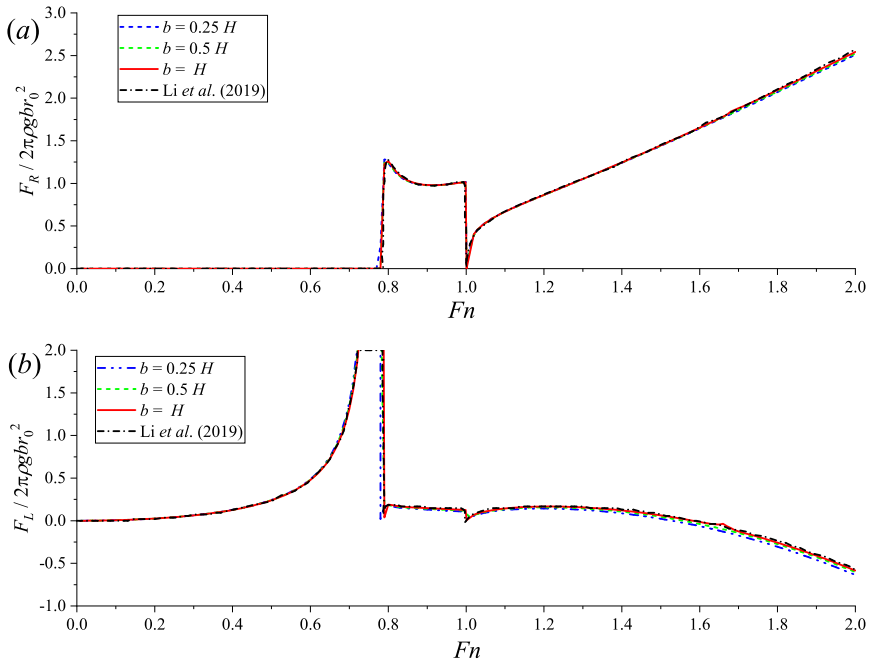

Figure 13: Hydrodynamic forces on the cylinder in an ice-covered channel with Free - Free edges at different channel widths. (*a*) Resistance; (*b*) Lift.
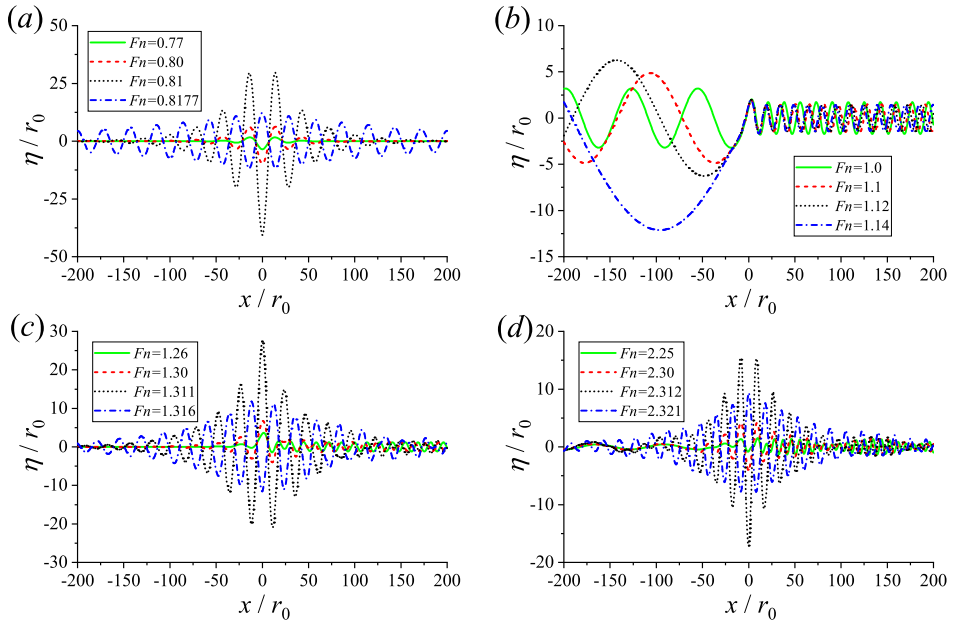
Figure 14: Ice sheet deflection η along $x-$axis due to a submerged horizontal cylinder when the ice sheet is under clamped-clamped edges. (a) $Fn < Fn_c^{(1)}$; (b) $Fn_c^{(1)} < Fn < Fn_0$; (c) $Fn_c^{(2)} < Fn < Fn_c^{(3)}$; ($d$) $Fn_c^{(4)} < Fn < Fn_c^{(5)}$. $Fn_c^{(1)} = 0.8180$, $Fn_c^{(2)} = 0.9981$, $Fn_c^{(3)} = 1.3177$, $Fn_c^{(4)} = 1.7682$, $Fn_c^{(5)} = 2.3230$, $Fn_0 = 1.1469$.

649   here, all the physical parameters are chosen as the same as those in Fig. 4 of Li *et al.* (2019).
650   The results of clamped - clamped edges are given in figure 12. When $b = 2H$, it can be seen
651   that the resistance and lift are significantly different from those in the two-dimensional case.
652   As b increases, the results tend to those without the tank wall. When $b = 8H$, very good
653   agreement can be observed between these two cases. It ought to point out at large b, for
654   example $b = 8H$, the critical Froude numbers $Fn_c^{(i)}$ ($i \geqslant 2$) still have effects. However the
655   effects are obvious only when Fn is very close to $Fn_c^{(i)}$, or the sharp variation of the force
656   is almost like a vertical line, although this line is not included in the figure. In figure 13,
657   the resistance and lift on the cylinder with free - free edges are provided. It can be observed
658   that even at small b, the results are already close to the two-dimensional ones. This suggests
659   that when doing model tests in an ice-covered tank, the free - free edges may resemble an
660   unbounded ocean better.

661   4.4. *Deflection of the ice sheet induced by a submerged horizontal cylinder*

662   We may also investigate the deflection of the ice sheet η due to a submerged horizontal
663   cylinder. The position of the centre line of cylinder is the same as that in Section 4.3. In figure
664   14, the hydroelastic waves along $x-$axis when the ice sheet is under clamped-clamped edges
665   are plotted. As can be observed, many features of the waves in figure 14 are similar to those in
666   figure 7, but there are also some differences. In figure 14(a), we can see that the wave profile
667   for $Fn < Fn_c^{(1)}$ is symmetric about $x = x_0$, which can be shown through (3.53)~(3.55), while
668   this is opposite to that in figure 7(a). As Fn increases, the ice deflection η at $x = 0$ reaches a
669   large negative value when Fn is close to $Fn_c^{(1)}$, then it will rapidly become a positive value
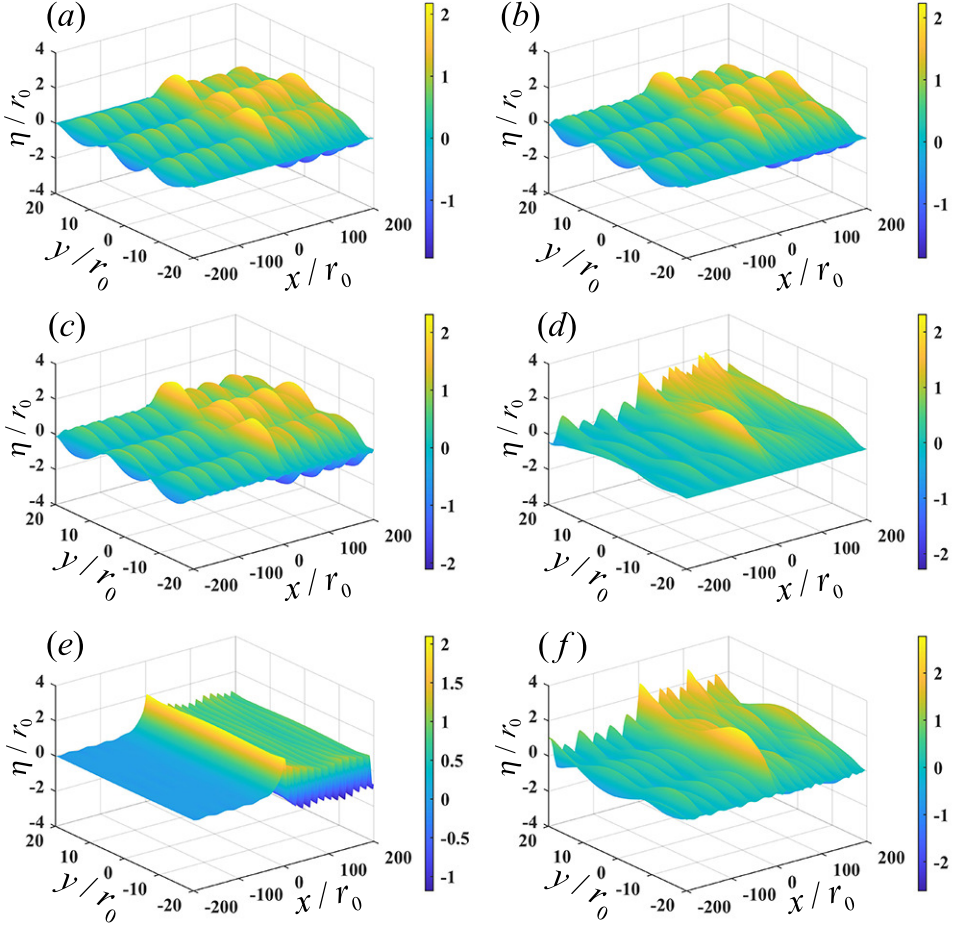
Figure 15: Wave patterns under different edge conditions when $Fn_c^{(3)} < Fn < Fn_c^{(4)}$.
(a) Clamped-Clamped edges, $Fn = 1.5$ ($Fn_c^{(3)} = 1.3177$ & $Fn_c^{(4)} = 1.7682$);
(b) Clamped-Simply supported edges, $Fn = 1.4$ ($Fn_c^{(3)} = 1.2569$ & $Fn_c^{(4)} = 1.6824$);
(c) Simply supported-Simply supported edges, $Fn = 1.3$
($Fn_c^{(3)} = 1.2012$ & $Fn_c^{(4)} = 1.6005$);
(d) Clamped-Free edges, $Fn = 1.3$ ($Fn_c^{(3)} = 1.0962$ & $Fn_c^{(4)} = 1.4454$);
(e) Free-Free edges, $Fn = 1.05$ ($Fn_c^{(3)} = 0.9486$ & $Fn_c^{(4)} = 1.1997$);
(f) Simply supported-Free edges, $Fn = 1.1$ ($Fn_c^{(3)} = 1.0561$ & $Fn_c^{(4)} = 1.3782$).

after Fn passes the critical point. Similar sudden change can be also observed in figures
14(c) and (d) when Fn is near $Fn_c^{(3)}$ and $Fn_c^{(5)}$. However, the deflection above the cylinder
in figure 14(c) before the critical point is a crest, while it is a trough in figures 14(a) and
(d). As discussed previously, the results from the linear theory might become qualitatively
inaccurate near one of the critical Froude numbers and the nonlinearity and other effects
may need to be taken into account. However, this is only within a very small range. Also the
critical Froude numbers predicted from the linear theory are still valid.

In order to show the influence of edge conditions on the wave profiles, typical wave patterns
under six different edge constraints when $Fn_c^{(3)} < Fn < Fn_c^{(4)}$ are presented in figure 15. For

679 waves under symmetric edges given in figures 15(a), (c) and (e), there is only one component
680 in the longitudinal wave at the downstream region, while the waves at the upstream region
681 contain two components. It can be found that the wave patterns under clamped-clamped and
682 simply supported-simply supported edges are relatively similar, but the wave pattern under
683 free-free is quite different. In figure 15(e), we can see that the downstream wave under free-
684 free edges is not as obvious as that under other two symmetric edges. Similar phenomenon
685 can be also observed from the transverse waves in figures 15(a), (c) and (e). From these
686 result, we may infer that an ice-coved channel with free-free edges is closer to an unbounded
687 region when compared to those with other edge restraints. For waves under asymmetric edge
688 restraints shown in figures 15(b), (d) and (f). The longitudinal waves at the downstream
689 region consist of two components, while the waves at the upstream region containing three
690 components. Compared with the wave profiles under clamped-simply supported edges shown
691 in figure 15(b), the asymmetry of the transverse waves is more obvious in cases with a free
692 edge given in figures 15(d) and (f).

5. Conclusions

694 The interaction of a uniform current with a submerged horizontal circular cylinder in an
695 ice-covered channel is studied analytically, the solution procedure is applicable to various
696 edge conditions. The three-dimensional Green function satisfying all boundary conditions
697 apart from that on the body surface is first derived. By using this, the potential due to sources
698 distributed along the centre line of the cylinder is obtained, from which the potentials due
699 to multipoles are constructed directly by differentiating the position of the centre line. The
700 velocity potential for a submerged circular cylinder is written in terms of a summation of
701 these multipoles.

702 From the solution of the Green function, it is confirmed that there is an infinite number of
703 critical Froude numbers $Fn_c^{(i)}$ ($i = 1, 2, 3...$) and another one Fn_0 which corresponds to the
704 case of $Fn_0 = 1$ in the two-dimensional problem where there are only two critical Froude
705 numbers. This is consistent with what has been noticed in the previous work (Khabakhpasheva
706 *et al.* 2019). There will be no wave propagating to infinity when $Fn < Fn_c^{(1)}$. When $Fn_c^{(i)} <$
707 $Fn < Fn_c^{(i+1)}$ and $Fn < Fn_0$, there will be $2i$ waves, and i waves are at downstream region
708 with group velocity smaller than the current speed, while the other i waves with larger group
709 velocity are at upstream region. When $Fn_c^{(i)} < Fn < Fn_c^{(i+1)}$ and $Fn > Fn_0$, one downstream
710 wave will disappear, and there will be $i - 1$ waves at downstream. For infinite water depth,
711 the effect of Fn_0 does not exist. When $\widetilde{Fn}_c^{(i)} < Fn < \widetilde{Fn}_c^{(i+1)}$, there are always $2i$ waves, with
712 i waves at $x = -\infty$ and $x = +\infty$ respectively.

713 In the cases of symmetric edge constraints, the symmetric and anti-symmetric transverse
714 modes are completely independent. The former corresponds to the roots of $Fn = Fn^{(2i-1)}$
715 ($i \geqslant 1$), while the latter corresponds to the solutions of $Fn = Fn^{(2i)}$. If the flow itself is
716 symmetric about $y = 0$, the waves due to the roots of $Fn = Fn^{(2i)}$ will not exist. In general,
717 the symmetric and anti-symmetric modes always coexist, and they are fully coupled. When
718 $Fn_c^{(i-1)} < Fn < Fn_c^{(i)}$ ($i \geqslant 2$), the contribution of the i-th transverse wave mode to the overall
719 wave profile will be significant.

720 The ice sheet deflection due to a submerged horizontal circular cylinder shows that the
721 hydroelastic wave is symmetric about $x = x_0$ and only exists in the region near the cylinder
722 when $Fn < Fn_c^{(1)}$. When Fn is near $Fn_c^{(1)}$, there is a sudden change in the wave above
723 the cylinder, which is similar to that of the two-dimensional case (Li *et al.* 2019). As Fn
724 increases, this phenomenon can be also observed near other critical points which do not

exist in the two-dimensional case. The three-dimensional wave pattern also indicates that it can be greatly affected by the edge conditions. The resistance on the cylinder is zero when $Fn < Fn_c^{(1)}$, while the lift is nonzero. When Fn increases and passes each critical Froude number, the forces change very rapidly. Under different edge conditions, the change is very different.

Acknowledgements

Declaration of interests

The authors report no conflict of interest.

Appendix A. Elements of the matrix $[\mathcal{A}]$ and columns $[\mathcal{B}]$ & $[C]$ under clamped-clamped edges condition

Applying the clamped-clamped edge condition shown in (2.11) to ξ, we have

$$\left. \begin{array}{r} c_0 - bc_1 + b^2 c_2 - b^3 c_3 + \dfrac{a_0}{24} b^4 + \displaystyle\sum_{m=1}^{+\infty} \dfrac{a_m}{\sigma_m^4} = 0 \\[2mm] c_1 - 2bc_2 + 3b^2 c_3 - \dfrac{a_0}{6} b^3 = 0 \\[2mm] c_0 + bc_1 + b^2 c_2 + b^3 c_3 + \dfrac{a_0}{24} b^4 + \displaystyle\sum_{m=1}^{+\infty} (-1)^m \dfrac{a_m}{\sigma_m^4} = 0 \\[2mm] c_1 + 2bc_2 + 3b^2 c_3 + \dfrac{a_0}{6} b^3 = 0 \end{array} \right\} . \tag{A 1}$$

Substituting (3.15) and (3.18a) into (A 1), the coefficients of matrix $[\mathcal{A}]$ and column $[\mathcal{B}]$ can then be given as

$$\left. \begin{array}{l} \mathcal{A}_{0j} = \delta_{0j} - \delta_{1j} b + \delta_{2j} b^2 - \delta_{3j} b^3 + \dfrac{\alpha_{0,j}}{24} b^4 + \displaystyle\sum_{m=1}^{+\infty} \dfrac{\alpha_{m,j}}{\sigma_m^4} \\[3mm] \mathcal{A}_{1j} = \delta_{1j} - \delta_{2j} 2b + \delta_{3j} 3b^2 - \dfrac{\alpha_{0,j}}{6} b^3 \\[3mm] \mathcal{A}_{2j} = \delta_{0j} + \delta_{1j} b + \delta_{2j} b^2 + \delta_{3j} b^3 + \dfrac{\alpha_{0,j}}{24} b^4 + \displaystyle\sum_{m=1}^{+\infty} (-1)^m \dfrac{\alpha_{m,j}}{\sigma_m^4} \\[3mm] \mathcal{A}_{3j} = \delta_{1j} + \delta_{2j} 2b + \delta_{3j} 3b^2 + \dfrac{\alpha_{0,j}}{6} b^3 \end{array} \right\} , \tag{A 2}$$

$$\mathcal{B}_j = -\mathrm{i} \sum_{m=0}^{+\infty} \frac{\rho U k \cosh K_m(z_0 + H) \cos \sigma_m(y_0 + b)}{(1 + \delta_{m0}) b \Delta_m \cosh K_m H} v_{m,j}, \quad j = 0 \sim 3, \tag{A 3}$$

747 where

$$
v_{m,j} = \begin{cases} \delta_{0j}\left[\dfrac{1-\delta_{m0}}{\sigma_m^4} + \delta_{m0}\left(\dfrac{b^4}{24} + \sum_{l=1}^{+\infty}\dfrac{\gamma_l}{\sigma_l^4}\right)\right] - \delta_{1j}\delta_{m0}\dfrac{b^3}{6} \\[3mm] + \delta_{2j}\left[\dfrac{(1-\delta_{m0})(-1)^m}{\sigma_m^4} + \delta_{m0}\left(\dfrac{b^4}{24} + \sum_{l=1}^{+\infty}\dfrac{(-1)^l\gamma_l}{\sigma_l^4}\right)\right] + \delta_{3j}\delta_{m0}\dfrac{b^3}{6} \end{cases}.
\tag{A 4}
$$

749 Based on (A 2) and (A 3), the solution of c_i of (3.21) can be obtained as

$$
c_i = -\mathrm{i}\sum_{m=0}^{+\infty}\frac{\rho U k \cosh K_m(z_0 + H)\cos\sigma_m(y_0 + b)}{(1+\delta_{m0})b|\mathcal{A}|\Delta_m\cosh K_m H}c'_{m,i}, \quad i = 0 \sim 3,
\tag{A 5}
$$

751 where $c'_{m,i} = |\mathcal{A}| \times c_{m,i}$, $c_{m,i}$ is the solution of $[\mathcal{A}][C_m] = [v_m]$, $[v_m]$ is a known column
752 containing coefficients $v_{m,i}$ ($i = 0 \sim 3$), $[C_m]$ is an unknown column containing $c_{m,i}$.
753 Substituting (3.20) into (A 1), the matrix equation (3.21) can be further split into two 2×2
754 sub ones, which can be written as

$$
[\mathcal{A}^S]\begin{bmatrix} c_0 \\ c_2 \end{bmatrix} = [\mathcal{B}^S] \quad \text{and} \quad [\mathcal{A}^A]\begin{bmatrix} c_1 \\ c_3 \end{bmatrix} = [\mathcal{B}^A],
\tag{A 6}
$$

756 or symmetric and anti-symmetric modes are fully uncoupled. The elements of matrixes
757 $[\mathcal{A}^S]$, $[\mathcal{A}^A]$ and column $[\mathcal{B}^S]$, $[\mathcal{B}^A]$ can be expressed as

$$
\left.\begin{aligned}
\mathcal{A}^S_{0j} &= \delta_{0j} + \delta_{1j}b^2 + \frac{\alpha_{0,2j}}{24}b^4 + \sum_{m=1}^{+\infty}\frac{\alpha_{2m,2j}}{\sigma_{2m}^4} \\
\mathcal{A}^S_{1j} &= 2\delta_{1j}b + \frac{\alpha_{0,2j}}{6}b^3
\end{aligned}\right\} \text{ and } \left.\begin{aligned}
\mathcal{A}^A_{0j} &= \delta_{0j}b + \delta_{1j}b^3 + \sum_{m=1}^{+\infty}\frac{\alpha_{2m-1,2j+1}}{\sigma_{2m-1}^4} \\
\mathcal{A}^A_{1j} &= \delta_{0j} + 3\delta_{1j}b^2
\end{aligned}\right\},
\tag{A 7}
$$

759 and

$$
\left.\begin{aligned}
\mathcal{B}^S_j &= -\mathrm{i}\sum_{m=0}^{+\infty}\frac{\rho U k(-1)^m\cosh K_{2m}(z_0 + H)\cos\sigma_{2m}y_0}{(1+\delta_{m0})b\Delta_{2m}\cosh K_{2m}H}v^S_{m,j} \\
\mathcal{B}^A_j &= \mathrm{i}\sum_{m=0}^{+\infty}\frac{\rho U k(-1)^m\cosh K_{2m+1}(z_0 + H)\sin\sigma_{2m+1}y_0}{b\Delta_{2m+1}\cosh K_{2m+1}H}v^A_{m,j}
\end{aligned}\right\}, \quad j = 0, 1
\tag{A 8}
$$

761 with

$$
v^S_{m,j} = \delta_{0j}\left[\frac{1-\delta_{m0}}{\sigma_{2m}^4} + \delta_{m0}\left(\frac{b^4}{24} + \sum_{l=1}^{+\infty}\frac{\gamma_{2l}}{\sigma_{2l}^4}\right)\right] + \delta_{1j}\delta_{m0}\frac{b^3}{6} \quad \text{and} \quad v^A_{m,j} = \frac{\delta_{0j}}{\sigma_{2m+1}^4}.
\tag{A 9}
$$

763 $|\mathcal{A}|$ can be further obtained as

$$
|\mathcal{A}| = 4|\mathcal{A}^S||\mathcal{A}^A|.
\tag{A 10}
$$

Appendix B. Symmetry property of the Green function

766 Let $G_0 = G(x, y, z, x_0, y_0, z_0)$ and $G_1 = G(x, y, z, x_1, y_1, z_1)$, and correspondingly, $\xi_0 = \xi(x, y, x_0, y_0, z_0)$ and $\xi_1 = \xi(x, y, x_1, y_1, z_1)$. At $x \to +\infty$, the Green function and the wave
768 elevation can be expressed as

$$
G_0 = \mathrm{Re}\left\{\sum_{j=0}^{S}\frac{G_0^{(j)}(y, z)}{k_j}e^{-\mathrm{i}k_j(x-x_0)}\right\} \quad \text{and} \quad G_1 = \mathrm{Re}\left\{\sum_{l=0}^{S}\frac{G_1^{(l)}(y, z)}{k_l}e^{-\mathrm{i}k_l(x-x_1)}\right\},
\tag{B 1}
$$

$$\xi_0 = \mathrm{Re}\left\{\sum_{j=0}^{S}\xi_0^{(j)}(y)e^{-\mathrm{i}k_j(x-x_0)}\right\} \quad \text{and} \quad \xi_1 = \mathrm{Re}\left\{\sum_{l=0}^{S}\xi_1^{(l)}(y)e^{-\mathrm{i}k_l(x-x_1)}\right\}, \tag{B 2}$$

where $k_0 \to 0$ and k_j ($j = 1 \sim S$) denotes the wave number of the component j, and the summation contains only those wave components with group velocity larger than U. The terms of $j = 0$ in (B 1) are related to the 'blockage parameter', as discussed for example in Newman (1969) and Mei & Chen (1976) in the two dimensional case. However, for a submerged body, there should be no net flow being created. Therefore, the blockage parameter is a constant. Its derivative will be zero and no flow will be created by the constant. (B 1) is due to a source which does generate flow into the fluid domain. This will continue at infinity, which is reflected by the terms of $j = 0$ of (B 1).

Although G and ξ involve only the real part, we may use the whole complex function here. Substituting (B 1) and (B 2) into (2.6) and (2.7), the boundary conditions of $G_0^{(j)}$ and $\xi_0^{(j)}$ on ice sheet can be established as

$$\mathrm{i}\left[(Lk_j^4 + \rho g)\xi_0^{(j)} - 2Lk_j^2\frac{d^2\xi_0^{(j)}}{dy^2} + L\frac{d^4\xi_0^{(j)}}{dy^4}\right] = \rho U G_0^{(j)}, \quad j = 0 \sim S, \quad z = 0, \tag{B 3}$$

$$\mathrm{i}k_j^2 U\xi_0^{(j)} = \frac{\partial G_0^{(j)}}{\partial z}, \quad j = 0 \sim S, \quad z = 0. \tag{B 4}$$

Similar procedure can be adopted at $x \to -\infty$. Applying the Green's second identity, we have

$$G(x_1, y_1, z_1, x_0, y_0, z_0) - G(x_0, y_0, z_0, x_1, y_1, z_1) = \oiint_{S}\left(G_0\frac{\partial G_1}{\partial n} - G_1\frac{\partial G_0}{\partial n}\right)dS, \tag{B 5}$$

where S is comprised of the seabed S_H, two vertical channel walls S_w, ice sheet S_I and two vertical surfaces $S_{\pm\infty}$ at $x \to \pm\infty$, respectively. As $\partial G_0/\partial n$ and $\partial G_1/\partial n$ are zero on S_H and S_w, only the integrals over S_I and $S_{\pm\infty}$ need to be kept.

For the integral at S_I, using (2.6), (2.7) and integration by parts, this gives

$$I_I = \iint_{S_I}\left(G_0\frac{\partial G_1}{\partial z} - G_1\frac{\partial G_0}{\partial z}\right)dS$$
$$= -U\int_{-b}^{b}(G_0\xi_1 - G_1\xi_0)|_{x\to-\infty}^{x\to+\infty}\,dy + \frac{L}{\rho}\iint_{S_I}(\xi_1\nabla^4\xi_0 - \xi_0\nabla^4\xi_1)dS. \tag{B 6}$$

Employing (A.3) in Ren *et al.* (2018*b*), I_I can be written as

$$I_I = -U\int_{-b}^{b}(G_0\xi_1 - G_1\xi_0)|_{x\to-\infty}^{x\to+\infty}\,dy$$
$$+ \frac{L}{\rho}\oint_{\mathcal{T}}\left(\xi_1\frac{\partial}{\partial n}\nabla^2\xi_0 - \frac{\partial\xi_1}{\partial n}\nabla^2\xi_0 - \xi_0\frac{\partial}{\partial n}\nabla^2\xi_1 + \frac{\partial\xi_0}{\partial n}\nabla^2\xi_1\right)dl, \tag{B 7}$$

where $\mathcal{T}$ is comprised of the lines $x = \pm\infty$ and $y = \pm b$. Using (B 1)~(B 3) and integrating

by parts again, I_I can be further written as

$$
I_I = \left\{
\begin{aligned}
&\frac{\mathrm{i}L}{\rho} \sum_{j=0}^{S} \sum_{l=0}^{S} e^{-\mathrm{i}[k_j(x-x_0)+k_l(x-x_1)]} \left[
\begin{aligned}
&\left(\xi_{1y}^{(l)}\xi_{0yy}^{(j)}/k_j - \xi_{0y}^{(j)}\xi_{1yy}^{(l)}/k_l\right) \\
&- \left(\xi_1^{(l)}\xi_{0yyy}^{(j)}/k_j - \xi_0^{(j)}\xi_{1yyy}^{(l)}/k_l\right)
\end{aligned}
\right]\Bigg|_{y=-b}^{y=b}\Bigg|_{x\to-\infty}^{x\to+\infty} \\
&+ \frac{L}{\rho} \int_{-\infty}^{+\infty} \left[
\begin{aligned}
&\left(\xi_1\xi_{0yyy} - \xi_0\xi_{1yyy}\right) - \left(\xi_{1y}\xi_{0yy} - \xi_{0y}\xi_{1yy}\right) \\
&- 2\left(\xi_{1x}\xi_{0xy} - \xi_{0x}\xi_{1xy}\right)
\end{aligned}
\right]\Bigg|_{y=-b}^{y=b} dx
\end{aligned}
\right\}
$$
(B 8)

Invoking the edge conditions in (2.11), it can be shown $I_I = 0$ for any of these edge constraints.

For the integral over $S_{\pm\infty}$, we can consider $S_{+\infty}$ as an example, as the integral over $S_{-\infty}$ can be done in a similar way. Substituting (B 1) into the integral at $S_{+\infty}$, we have

$$
\begin{aligned}
I_{+\infty} &= \iint_{S_{+\infty}} \left(G_0 \frac{\partial G_1}{\partial x} - G_1 \frac{\partial G_0}{\partial x}\right) dS \\
&= \sum_{j=0}^{S} \sum_{l=0}^{S} e^{-\mathrm{i}[k_j(x-x_0)+k_l(x-x_1)]} \iint_{S_{+\infty}} \left(\frac{1}{k_l} - \frac{1}{k_j}\right) G_0^{(j)} G_1^{(l)} dS.
\end{aligned}
$$
(B 9)

Since G_0 and G_1 is governed by the Laplace equation at $x \to +\infty$, we have

$$
\left.
\begin{aligned}
\nabla_{yz}^2 G_0^{(j)} &= k_j^2 G_0^{(j)} \\
\nabla_{yz}^2 G_1^{(l)} &= k_j^2 G_1^{(l)}
\end{aligned}
\right\},
$$
(B 10)

where $\nabla_{yz}^2 = \partial^2/\partial y^2 + \partial^2/\partial z^2$ denotes the Laplace operator at $O - yz$ plane. Substituting (B 10) into (B 9) and applying Green's second identity, we obtain

$$
\begin{aligned}
I_{+\infty} &= \mathrm{i} \sum_{j=0}^{S} \sum_{l=0}^{S} \frac{e^{-\mathrm{i}[k_j(x-x_0)+k_l(x-x_1)]}}{k_j k_l(k_j + k_l)} \iint_{S_{+\infty}} \left(G_1^{(l)}\nabla_{yz}^2 G_0^{(j)} - G_0^{(j)}\nabla_{yz}^2 G_1^{(l)}\right) dS \\
&= \mathrm{i} \sum_{j=0}^{S} \sum_{l=0}^{S} \frac{e^{-\mathrm{i}[k_j(x-x_0)+k_l(x-x_1)]}}{k_j k_l(k_j + k_l)} \oint_{\mathcal{L}_{+\infty}} \left(G_1^{(l)}\frac{\partial G_0^{(j)}}{\partial n} - G_0^{(j)}\frac{\partial G_1^{(l)}}{\partial n}\right) dS,
\end{aligned}
$$
(B 11)

where $\mathcal{L}_{+\infty}$ is comprised of lines $y = \pm b$, $z = 0$ and $z = -H$. Applying (2.9), (2.10), (B 3) and (B 4), we have

$$
I_{+\infty} = \frac{\mathrm{i}L}{\rho} \sum_{j=0}^{S} \sum_{l=0}^{S} \frac{e^{-\mathrm{i}[k_j(x-x_0)+k_l(x-x_1)]}}{k_l + k_j} \int_{-b}^{+b} \left[
\begin{aligned}
&2k_j k_l\left(\xi_0^{(j)}\xi_{1yy}^{(l)} - \xi_1^{(l)}\xi_{0yy}^{(j)}\right) \\
&- \left(k_j\xi_0^{(j)}\xi_{1yyyy}^{(l)}/k_l - k_l\xi_1^{(l)}\xi_{0yyyy}^{(j)}/k_j\right)
\end{aligned}
\right] dy.
$$
(B 12)

Using integration by parts and edge conditions in (2.11), we have $I_{+\infty} = 0$, similarly $I_{-\infty} = 0$. This means that the integral at right hand-side of (B 5) is equal to 0, which gives

$$
G(x_1, y_1, z_1, x_0, y_0, z_0) = G(x_0, y_0, z_0, x_1, y_1, z_1).
$$
(B 13)

Appendix C. Far-field formula of the resistance

The formula of the resistance can be written as (Wu 1995)

$$
F_R = -\frac{1}{2}\rho \iint_{S_B} \left(\phi_x \frac{\partial \phi}{\partial n} - \phi \frac{\partial \phi_x}{\partial n}\right) dS,
$$
(C 1)

Using Green's second identity, it can be converted as

$$F_R = \frac{1}{2}\rho \iint_{S_I+S_{\pm\infty}} \left(\phi_x \frac{\partial \phi}{\partial n} - \phi \frac{\partial \phi_x}{\partial n}\right) dS. \tag{C2}$$

It is noted that the integral in (C2) can be treated in a similar way as shown in appendix B. This gives

$$F_R = \begin{bmatrix} \dfrac{1}{2}\rho \displaystyle\int_{-H}^{0} dz \int_{-b}^{b} \left(\dfrac{\partial \phi}{\partial x}\dfrac{\partial \phi}{\partial x} - \phi \dfrac{\partial^2 \phi}{\partial x^2}\right)\bigg|_{x\to-\infty}^{x\to+\infty} dy \\[2mm] -\dfrac{1}{2}\rho U \displaystyle\int_{-b}^{b} \left(\eta\dfrac{\partial \phi}{\partial x} - \phi\dfrac{\partial \eta}{\partial x}\right)\bigg|_{x\to-\infty}^{x\to+\infty}\bigg|_{z=0} dy \\[2mm] +\dfrac{L}{2} \displaystyle\int_{-b}^{b} \left[\left(\eta\dfrac{\partial^4 \eta}{\partial x^4} - \dfrac{\partial \eta}{\partial x}\dfrac{\partial^3 \eta}{\partial x^3}\right) - \left(\dfrac{\partial \eta}{\partial x}\dfrac{\partial^3 \eta}{\partial x^3} - \dfrac{\partial^2 \eta}{\partial x^2}\dfrac{\partial^2 \eta}{\partial x^2}\right)\right]\bigg|_{x\to-\infty}^{x\to+\infty} dy \\[2mm] +\dfrac{L}{U} \displaystyle\int_{-b}^{b} \left(\eta\dfrac{\partial^4 \phi}{\partial x^3 \partial z} + \eta\dfrac{\partial \phi}{\partial x \partial z^3} - \dfrac{\partial \eta}{\partial x}\dfrac{\partial^3 \phi}{\partial x^2 \partial z} - \dfrac{\partial \eta}{\partial x}\dfrac{\partial \phi}{\partial z^3}\right)\bigg|_{x\to-\infty}^{x\to+\infty} dy \end{bmatrix}. \tag{C3}$$

Based on (3.40) and (3.53), the asymptotic expression of ϕ and η at $x\to+\infty$ can be written as:

$$\phi = \text{Re}\left\{\sum_{s=1}^{S}\sum_{n=0}^{+\infty}\chi_s \frac{\left[\mathscr{B}_{s,n}^{(1)} e^{\mathrm{i}k_s(x-x_0)} + \mathscr{B}_{s,n}^{(2)} e^{-\mathrm{i}k_s(x-x_0)}\right] k_s \cosh K_{n,s}(z+H)\cos\sigma_n(y+b)}{K_{n,s}\sinh K_{n,s}H}\right\}$$
$$+ \text{sgn}(x)\phi^{(0)}, \tag{C4}$$

$$\eta = -\frac{1}{U}\text{Im}\left\{\sum_{s=1}^{S}\sum_{n=0}^{+\infty}\chi_s\left[\mathscr{B}_{s,n}^{(1)} e^{\mathrm{i}k_s(x-x_0)} - \mathscr{B}_{s,n}^{(2)} e^{-\mathrm{i}k_s(x-x_0)}\right]\cos\sigma_n(y+b)\right\}, \tag{C5}$$

where

$$\begin{aligned}\mathscr{B}_{s,n}^{(1)} &= -\mathrm{i}\rho U \sum_{n'=0}^{+\infty}\sum_{m=1}^{+\infty} \frac{r_0^m f_{n',m}\tau_{n,n'}(k_s)E_{n',m}(k_s,z_0)}{2^m(m-1)!\Delta_{n'}(k_s)|\mathscr{A}|'(k_s)\cosh K_{n',s}H} \\[2mm] \mathscr{B}_{s,n}^{(2)} &= \mathrm{i}\rho U \sum_{n'=0}^{+\infty}\sum_{m=1}^{+\infty} \frac{r_0^m f_{n',m}\tau_{n,n'}(k_s)E_{n',m}(-k_s,z_0)}{2^m(m-1)!\Delta_{n'}(k_s)|\mathscr{A}|'(k_s)\cosh K_{n',s}H}\end{aligned}, \tag{C6}$$

$K_{n,s} = \sqrt{k_s^2 + \sigma_n^2}$, $\tau_{n,n'}(k) = \sum_{j=0}^{3}\beta_{n,j}c'_{n',j}$, and the summation of s contains only those wave components with group velocity larger than U. χ_s is related to the integration path $\mathscr{L}$ in (3.38c) and (3.55c), when $\mathscr{L}$ passes over (under) the singularity at k_s, the corresponding wave component will propagate to $x=+\infty$ ($x=-\infty$), and $\chi_s = -1$ ($\chi_s = +1$). Therefore, $\chi_s = -1$ in (C4) and (C5). Similar procedure can be also adopted at $x\to-\infty$. Substituting (C4) and (C5) into (C3), we have:

$$F_R = -\frac{b}{4U^2}\sum_{s=1}^{S}\sum_{n=0}^{+\infty}(1+\delta_{n0})\chi_s\left|\mathscr{B}_{s,n}^{(1)} + \bar{\mathscr{B}}_{s,n}^{(2)}\right|^2 \times \begin{bmatrix} \rho U^2 k_s^2\left(H + \sinh 2K_{n,s}H/2K_{n,s}\right) \\ -\rho U^2 K_{n,s}\sinh 2K_{n,s}H \\ +4LK_{n,s}^4\sinh^2 K_{n,s}H \end{bmatrix}, \tag{C7}$$

It should be noted that the summation of s in (C7) contains all the wave components.

REFERENCES

ABRAMOWITZ, M. & STEGUN, I. A. 1970 *Handbook of mathematical functions with formulas, graphs, and mathematical tables*, , vol. 55. US Government Printing Office.

BALMFORTH, N. J. & CRASTER, R. V. 1999 Ocean waves and ice sheets. *Journal of Fluid Mechanics* **395**, 89–124.

BENNETTS, L. G. & WILLIAMS, T. D. 2010 Wave scattering by ice floes and polynyas of arbitrary shape. *Journal of Fluid Mechanics* **662**, 5–35.

BROCKLEHURST, P., KOROBKIN, A. A. & PĂRĂU, E. I. 2011 Hydroelastic wave diffraction by a vertical cylinder. *Philosophical Transactions of the Royal Society A: Mathematical, Physical and Engineering Sciences* **369** (1947), 2832–2851.

DAS, D. & MANDAL, B. N. 2008 Water wave radiation by a sphere submerged in water with an ice-cover. *Archive of Applied Mechanics* **78** (8), 649–661.

DIŞIBÜYÜK, N. B., KOROBKIN, A. A. & YILMAZ, O. 2020 Diffraction of flexural-gravity waves by a vertical cylinder of non-circular cross section. *Applied Ocean Research* **101**, 102234.

EVANS, D. V. & PORTER, R. 1997 Near-trapping of waves by circular arrays of vertical cylinders. *Applied Ocean Research* **19** (2), 83–99.

EVANS, D. V. & PORTER, R. 2003 Wave scattering by narrow cracks in ice sheets floating on water of finite depth. *Journal of Fluid Mechanics* **484**, 143.

FOX, C. & SQUIRE, V. A. 1994 On the oblique reflexion and transmission of ocean waves at shore fast sea ice. *Philosophical Transactions of the Royal Society of London. Series A: Physical and Engineering Sciences* **347** (1682), 185–218.

HAUSSLING, HJ & COLEMAN, RM 1979 Nonlinear water waves generated by an accelerated circular cylinder. *Journal of Fluid Mechanics* **92** (4), 767–781.

HAVELOCK, THOMAS HENRY 1936 The forces on a circular cylinder submerged in a uniform stream. *Proceedings of the Royal Society of London. Series A-Mathematical and Physical Sciences* **157** (892), 526–534.

KHABAKHPASHEVA, T. I., SHISHMAREV, K. & KOROBKIN, A. A. 2019 Large-time response of ice cover to a load moving along a frozen channel. *Applied Ocean Research* **86**, 154–165.

KOROBKIN, A. A., KHABAKHPASHEVA, T. I. & PAPIN, A. A. 2014 Waves propagating along a channel with ice cover. *European Journal of Mechanics-B/Fluids* **47**, 166–175.

LAMB, HORACE 1932 *Hydrodynamics*. Cambridge university press.

LI, Z. F., SHI, Y. Y. & WU, G. X. 2020*a* A hybrid method for linearized wave radiation and diffraction problem by a three dimensional floating structure in a polynya. *Journal of Computational Physics* p. 109445.

LI, Z. F., WU, G. X. & REN, K. 2020*b* Interactions of wave with a body floating in an open water channel confined by two semi-infinite ice sheets. *Submitted* .

LI, Z. F., WU, G. X. & REN, K. 2020*c* Wave diffraction by multiple arbitrary shaped cracks in an infinitely extended ice sheet of finite water depth. *Journal of Fluid Mechanics* **893**.

LI, Z. F., WU, G. X. & SHI, Y. Y. 2019 Interaction of uniform current with a circular cylinder submerged below an ice sheet. *Applied Ocean Research* **86**, 310–319.

LINTON, C. M. 1993 On the free-surface green's function for channel problems. *Applied Ocean Research* **15** (5), 263–267.

LINTON, C. M., EVANS, D. V. & SMITH, F. T. 1992 The radiation and scattering of surface waves by a vertical circular cylinder in a channel. *Philosophical Transactions of the Royal Society of London. Series A: Physical and Engineering Sciences* **338** (1650), 325–357.

LINTON, C. M. & MCIVER, P. 2001 *Handbook of mathematical techniques for wave/structure interactions*. CRC Press.

MEI, C. C. & CHEN, H. S. 1976 A hybrid element method for steady linearized free-surface flows. *International Journal for Numerical Methods in Engineering* **10** (5), 1153–1175.

MEYLAN, M. H. & SQUIRE, V. A. 1996 Response of a circular ice floe to ocean waves. *Journal of Geophysical Research: Oceans* **101** (C4), 8869–8884.

NEWMAN, J. N. 1969 Lateral motion of a slender body between two parallel walls. *Journal of Fluid Mechanics* **39** (1), 97–115.

NEWMAN, J. N. 2017 Trapped-wave modes of bodies in channels. *Journal of Fluid Mechanics* **812**, 178–198.

PORTER, R. 2019 The coupling between ocean waves and rectangular ice sheets. *Journal of Fluids and Structures* **84**, 171–181.

PORTER, R. & EVANS, D. V. 2007 Diffraction of flexural waves by finite straight cracks in an elastic sheet over water. *Journal of Fluids and Structures* **23** (2), 309–327.

REN, K., WU, G. X. & JI, C. Y. 2018*a* Diffraction of hydroelastic waves by multiple vertical circular cylinders. *Journal of Engineering Mathematics* **113** (1), 45–64.

REN, K., WU, G. X. & JI, C. Y. 2018*b* Wave diffraction and radiation by a vertical circular cylinder standing in a three-dimensional polynya. *Journal of Fluids and Structures* **82**, 287–307.

REN, K., WU, G. X. & LI, Z. F. 2020 Hydroelastic waves propagating in an ice-covered channel. *Journal of Fluid Mechanics* **886**.

SCULLEN, D & TUCK, EO 1995 Nonlinear free-surface flow computations for submerged cylinders. *Journal of Ship Research* **39** (3), 185–193.

SEMENOV, YA & WU, GX 2020 Free-surface gravity flow due to a submerged body in uniform current. *Journal of Fluid Mechanics* **883**.

SHISHMAREV, K., KHABAKHPASHEVA, T. & KOROBKIN, A. A. 2016 The response of ice cover to a load moving along a frozen channel. *Applied Ocean Research* **59**, 313–326.

SQUIRE, VERNON A 2007 Of ocean waves and sea-ice revisited. *Cold Regions Science and Technology* **49** (2), 110–133.

STUROVA, I. V. 2013 Unsteady three-dimensional sources in deep water with an elastic cover and their applications. *Journal of Fluid Mechanics* **730**, 392–418.

TIMOSHENKO, S. P. & WOINOWSKY-KRIEGER, S. 1959 *Theory of plates and shells*. McGraw-hill.

TUCK, EO 1965 The effect of non-linearity at the free surface on flow past a submerged cylinder. *Journal of Fluid Mechanics* **22** (2), 401–414.

URSELL, F. 1949 On the heaving motion of a circular cylinder on the surface of a fluid. *The Quarterly Journal of Mechanics and Applied Mathematics* **2** (2), 218–231.

URSELL, F. 1950 Surface waves on deep water in the presence of a submerged circular cylinder. i. In *Mathematical Proceedings of the Cambridge Philosophical Society*, , vol. 46, pp. 141–152. Cambridge University Press.

URSELL, F. 1951 Trapping modes in the theory of surface waves. In *Mathematical Proceedings of the Cambridge Philosophical Society*, , vol. 47, pp. 347–358. Cambridge University Press.

UTSUNOMIYA, T. & EATOCK TAYLOR, R. 1999 Trapped modes around a row of circular cylinders in a channel. *Journal of Fluid Mechanics* **386**.

WEHAUSEN, J. V. & LAITONE, E. V. 1960 Surface waves. In *Fluid Dynamics/Strömungsmechanik*, pp. 446–778. Springer.

WU, G. X. 1995 Radiation and diffraction by a submerged sphere advancing in water waves of finite depth. *Proceedings of the Royal Society of London. A. Mathematical and Physical and Engineering Sciences* **448** (1932), 29–54.

WU, G. X. 1998*a* Wave radiation and diffraction by a submerged sphere in a channel. *The Quarterly Journal of Mechanics and Applied Mathematics* **51** (4), 647–666.

WU, G. X. 1998*b* Wavemaking resistance on a submerged sphere in a channel. *Journal of Ship Research* **42** (01), 1–8.

WU, G. X. & EATOCK TAYLOR, R 1987 Hydrodynamic forces on submerged oscillating cylinders at forward speed. *Proceedings of the Royal Society of London. A. Mathematical and Physical and Engineering Sciences* **414** (1846), 149–170.